Electronic Supporting Information

A Zero-Field Single-Molecule Magnet with Luminescence Thermometry Capabilities Containing Soft Donors

Riccardo Marin,*[a]† Diogo Alves Gálico,[b]† Rezeda Gayfullina,[c] Jani O. Moilanen,[c] Luís D. Carlos,[d] Daniel Jaque[a],[e] and Muralee Murugesu*[b]

a. Nanomaterials for Bioimaging Group (nanoBIG), Departamento de Física de Materiales, Facultad de Ciencias, Universidad Autónoma de Madrid, C/ Francisco Tomás y Valiente 7, Madrid 28049, Spain.

b. Department of Chemistry and Biomolecular Sciences, University of Ottawa, Ottawa, Ontario K1N 6N5, Canada.

c. Department of Chemistry, University of Jyväskylä, Jyväskylä, FI-40014, Finland.

d. Phantom-g, CICECO – Aveiro Institute of Materials, Department of Physics, Universidade de Aveiro 3810-193 Aveiro, Portugal.

e. Nanomaterials for Bioimaging Group (nanoBIG), Instituto Ramón y Cajal de Investigación Sanitaria, Hospital Ramón y Cajal, Ctra. De Colmenar Viejo, Km. 9100, 28034 Madrid, Spain

TABLE OF CONTENT

1. Materials and Methods

Chemicals. Dysprosium nitrate pentahydrate ($Dy(NO_3)_3{\cdot}5H_2O$, 99.9%, Alfa Aesar), thiobenzoic acid (Htba, >93%, TCI), potassium carbonate (K_2CO_3, Fisher Scientific), 1,10-phenanthroline (phen, Alfa Aesar), chloroform, deionized water.

Synthesis of Ktba. The potassium salt of the thioacid was synthesized according to a method adapted from the literature.[1] Briefly, 5 mL of Htba (64.2 mmol) was added to a stirring solution of 4.4 g (32.1 mmol) of K_2CO_3 in 100 mL of deionized water. The yellow solution was stirred for 2 h, filtered, and the water was removed with the aid of a rotary evaporator. A beige solid was collected, redissolved in 50 mL of water, filtered, and dried again. K(tba) was collected as a slightly yellow powder and recrystallized from hot ethanol, yielding bright yellow crystals.

Synthesis of $[Dy(tba)_3phen]{\cdot}CH_2Cl_2$. Three mmoles (528.9 mg) of Ktba and 1 mmol of phen (180.2 mg) were added to a 25-mL beaker along with 7.5 mL of water. The ligand solution was brought to 80 ºC until all the solids were dissolved. The solution was then cooled to room temperature and 2 mL of a 0.5 M aqueous solution of $Dy(NO_3)_3{\cdot}5H_2O$ was added dropwise. Upon addition of the metal ion solution, a precipitate immediately formed. The mixture was kept under stirring for 1 h. The solid was filtered, washed three times with deionized water, and allowed to dry at room temperature overnight. Recrystallization of the complex was performed dissolving the solid in dichloromethane, filtering the clear solution and slowly evaporating the solvent. Yield: 32 %. **FTIR:** 3082 (w), 3059 (w), 2925 (w), 2856 (w), 1625 (w), 1591 (m), 1517 (m), 1463 (s), 1425 (s), 1344 (w), 1304 (m), 1257 (w), 1221 (s), 1167 (m), 1143 (w), 1103 (w), 1075 (w), 1027 (w), 1000 (w), 968 (s), 937 (w), 847 (m), 778 (m), 727 (m), 692 (m), 656 (w), 617 (w), 560 (m), 486 (m). **Chemical composition exp. (calc.):** C 48.91% (48.72%), H 3.16% (2.89%), N 3.33 % (3.34%), S 11.07% (11.48%).

Structural and physicochemical characterization. Single-crystal X-ray diffraction (SC-XRD) measurements were performed on a Kappa Apex II (X8 APEX) Single-crystal Diffractometer using a Mo source (λ = 0.7107 Å). Infrared spectra were obtained in transmission mode on a Spectrum Two instrument (Perkin Elmer) in the 450–4000 cm^{-1} range with 4 cm^{-1} resolution, preparing KBr tablets containing 1 wt% of the analysed material. Elemental analysis was carried out on a CHNS-932 (LECO) elemental analyser using 1 mg of sample, using the Dumas method, which is based on a direct oxidative combustion of the sample at 1000 °C.

Magnetic characterization. The magnetic susceptibility measurements were obtained using a Quantum Design SQUID magnetometer MPMS-XL7 operating between 1.8 and 300 K. DC and/or AC measurements were performed on 8.2 mg of a polycrystalline sample. The sample was restrained with silicon grease and wrapped in a polyethylene membrane. The sample was subjected to DC fields of -7 to 7 T, and a 3.78 Oe driving field was used for AC measurements. The magnetization data were collected at 100 K to check for ferromagnetic impurities that were absent in all samples. Diamagnetic corrections were applied for the sample holder and the inherent diamagnetism of the sample was estimated with the use of Pascals' constants.

Spectroscopic characterization. The photoluminescence data were obtained using a QuantaMaster 8075-21 Spectrofluorometer (Horiba). An ozone-free PowerArc energy 75-W xenon lamp was used as the radiation source. The excitation spectra were corrected in real time according to the lamp intensity and the optical system of the excitation monochromator using a silicon diode as a reference. The emission spectra were corrected according to the optical system of the emission monochromator and the photomultiplier response (Hamamatsu R13456 red extended PMT). Low-temperature measurements were performed with the sample mounted inside a closed cycle helium cryostat system CS202*E-DMX-1AL (Advanced Research Systems) controlled via a LakeShore 335 temperature controller. The spectrum in Figure 3C was fit using 10 Gaussian curves (2 hot bands and 8 Dy^{3+} $^6H_{15/2}$ Kramers doublets), refining peak position, width, and area of each component. All parameters were left free to vary.

2. Structural and chemical characterization of $[Dy(tba)_3phen]\cdot CH_2Cl_2$

Table S1. Crystallographic data and selected data collection parameters

	$[Dy(tba)_3phen]\cdot CH_2Cl_2$
Chemical formula	$C_{34}H_{25}Cl_2DyN_2O_3S_3$
Molecular weight (a.u.)	839.14
Crystal system	Monoclinic
Space group	$P\,2_1/c$
a, b, c (Å)	13.8693(4), 15.1532(4), 16.6644(5)
α, β, γ (º)	90, 106.6357(13), 90
V (Å^3)	3355.67(17)
Z	4
Calculated density	1.661
μ (mm^{-1})	2.610
Acquisition temperature (K)	250
Θ range for data acquisition (º)	1.53 – 25.35
Limiting indices	h = ±16, k = ±18, l = ±20
Data, restraints, parameters	6134, 70, 428
Goodness-of-fit	1.040
R_1, wR_2 (I > 2σ(I))	0.0205, 0.0424
R_1, wR_2 (all data)	0.0301, 0.0466

Table S2. Results of the SHAPE analysis for $[Dy(tba)_3phen]\cdot CH_2Cl_2$ relative to an idealized 8-vertex polyhedron. The best match is highlighted in **bold**.

SHAPE code	**Point group**	**Description**	**Values**
OP-8	D_{8h}	Octagon	28.245
HPY-8	C_{7v}	Heptagonal pyramid	23.739
HBPY-8	D_{6h}	Hexagonal bipyramid	13.935
CU-8	O_h	Cube	12.771
SAPR-8	D_{4d}	Square antiprism	4.709
TDD-8	***D_{2d}***	**Triangular dodecahedron**	**3.023**
JGBF-8	D_{2d}	Johnson gyrobifastigium (J26)	11.497
JETBPY-8	D_{3h}	Johnson elongated triangular bipyramid (J14)	24.390
JBTP-8	C_{2v}	Johnson biaugmented trigonal prism (J50)	4.180
BTPR-8	C_{2v}	Biaugmented trigonal prism	4.032
JSD-8	D_{2d}	Snub disphenoid (J84)	4.009
TT-8	T_d	Triakis tetrahedron	12.704
ETBPY-8	D_{3h}	Elongated trigonal bipyramid	22.256

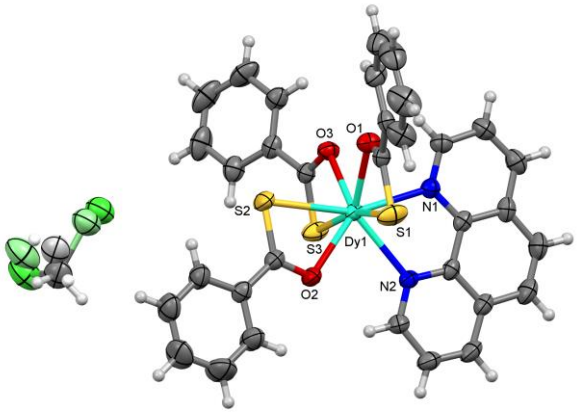

Figure S1. Partially labelled molecular structure of **1** with ellipsoids indicating the atomic displacement parameters (ADPs) for each atom in the structure. Colour code: Dy – cyan; O – red; S – yellow; N – blue; Cl – green; H – white.

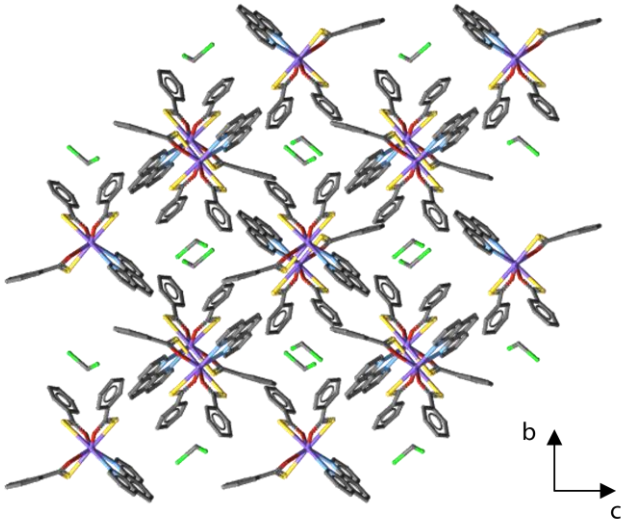

Figure S2. Molecular stacking seen along **a**. Colour code: Dy – purple; C – grey; O – red; S – yellow; N – blue; Cl – green.

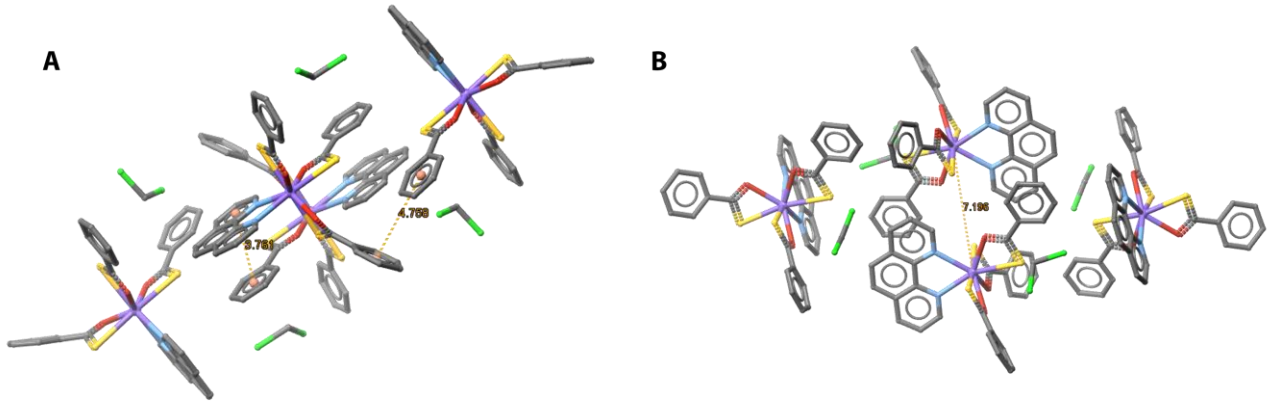

Figure S3. A) Shortest π···π distances in face-to-face and edge-to-face configurations. **B)** Shortest intramolecular Dy···Dy distance. Colour code: Dy – purple; C – grey; O – red; S – yellow; N – blue; Cl – green; centroids - orange.

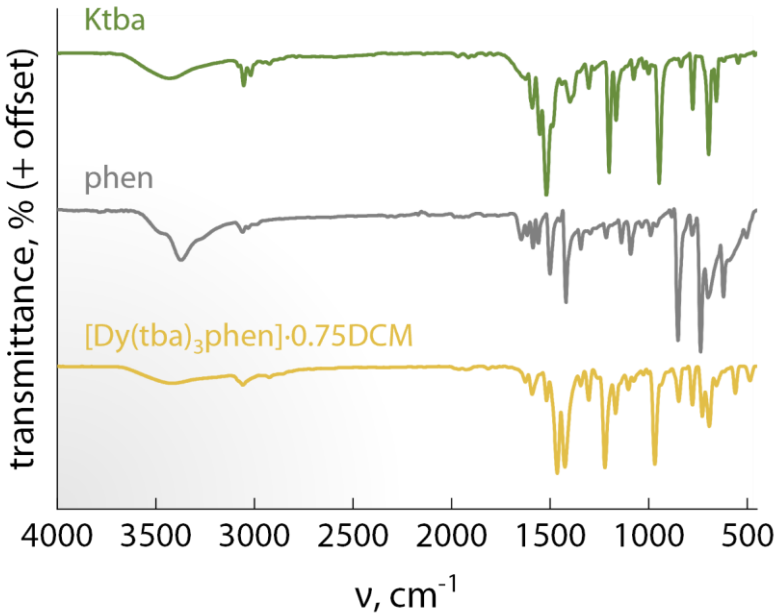

Figure S4. Fourier-transform infrared spectra of $[Dy(tba)_3phen]\cdot CH_2Cl_2$ (yellow) along with the ones of pristine ligands (Ktba – green -- and phen – grey).

3. Additional magnetic data

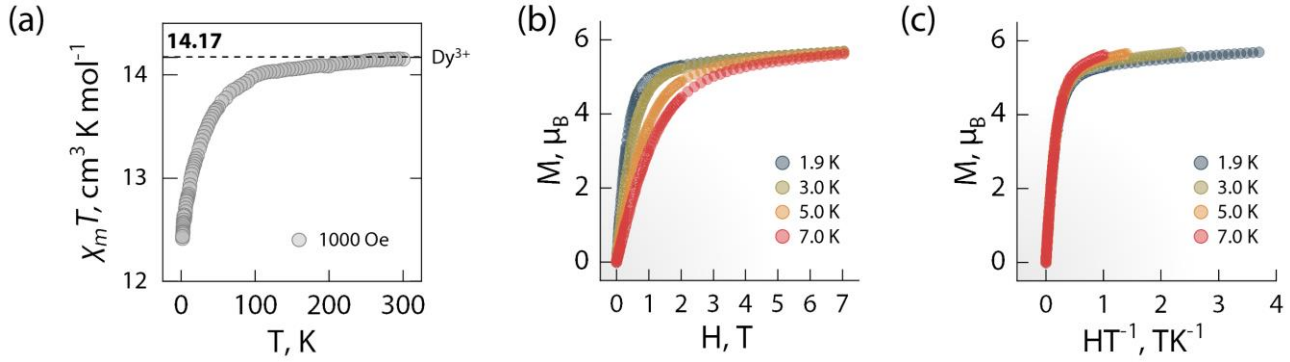

Figure S5. a) dc susceptibility of **1** under an applied field of 1000 Oe as a function of the temperature. **b)** Magnetization and **c)** reduced magnetization curves of **1** at the indicated temperatures.

Table S3: Best-fit parameters to the generalized Debye model for the temperature dependence of the the out-of-phase (χ'') magnetic susceptibility for **1**. Data collected without an external magnetic field.

T, K	χ_s	χ_t	α	τ
12	1.00E-05	2.11349	0.06399	5.41E-05
11	0.01568	2.2479	0.04843	1.21E-04
10	0.00513	2.47193	0.05015	2.70E-04
9.5	0.00411	2.61084	0.05987	4.05E-04
9	0.02975	2.77184	0.06209	6.21E-04
8.5	0.00459	2.86803	0.05422	9.58E-04
8	0.06238	3.12795	0.06503	0.00143
7.5	0.26338	2.98662	0.01602	0.00248
7	0.25775	3.04713	0.00651	0.00387
6.5	0.24536	3.32955	0.01516	0.00583
6	16.41996	19.58	0.0089	0.00932
5.5	16.81379	20.18621	0.0135	0.01492
5	17.2497	20.7503	0.01	0.0252
4.5	17.62756	21.37244	0.01756	0.04261
4	17.9918	22.0082	0.02822	0.07499
3.5	18.31731	22.68269	0.04985	0.13177
3	18.55916	23.44084	0.09233	0.22485
2.5	18.37734	24.36032	0.15305	0.34983
2	23.60645	31.54193	0.18362	0.48834
1.8	7.02063	16.22137	0.20251	0.55793

Table S4: Best-fit parameters to the generalized Debye model for the temperature dependence of the the out-of-phase (χ'') magnetic susceptibility for **1**. Data collected with an applied field of 500 Oe.

T, K	χ_s	χ_t	α	τ
12	0.06203	2.89138	0.06945	6.52E-05
11	6.78E-04	3.00384	0.05583	1.51E-04
10	0.00669	3.42967	0.06691	3.52E-04
9.5	0.0108	3.64246	0.07215	5.57E-04
9	0.03495	3.90544	0.07814	8.76E-04
8.5	0.04984	4.17115	0.08125	0.00139
8	0.0017	4.40569	0.07599	0.00221
7.5	0.07321	4.79185	0.07847	0.00353
7	0.0073	5.09198	0.07605	0.00566
6.5	0.00385	5.50336	0.07557	0.00931
6	0.0044	6.00903	0.078	0.01566
5.5	0.027	6.61372	0.08081	0.02776
5	0.34632	7.67348	0.08686	0.05186
4.5	0.54604	8.80675	0.09607	0.10474
4	0.95264	10.46428	0.11399	0.19558
3.5	0.00819	11.52743	0.15657	0.48014

Table S5: Best-fit parameters to the generalized Debye model for the field dependence of the the out-of-phase (χ'') magnetic susceptibility for **1**. Data collected at 5 K.

H, Oe	χ_s	χ_t	α	τ
0	0.0332	4.97094	0.17564	0.01272
50	0.02635	4.98097	0.17722	0.01288
100	0.09357	5.05704	0.17715	0.01417
150	0.03752	5.14345	0.14336	0.0171
200	0.08807	5.05941	0.16018	0.01918
250	0.04823	5.03344	0.1467	0.02216
300	0.0087	5.0031	0.1319	0.02497
350	0.00973	5.04137	0.12325	0.02732
400	3.03E-04	5.05705	0.11404	0.02932
450	2.30E-04	5.07302	0.10652	0.03092
500	0.02094	5.11236	0.10285	0.03194
600	0.28487	5.39043	0.09899	0.03286
800	0.00258	5.07976	0.10612	0.03183
1000	0.01589	5.03627	0.10985	0.03113
1200	0.23753	5.26136	0.1075	0.0329
1400	0.00217	5.01615	0.10828	0.03448
1600	0.16032	5.13858	0.10972	0.03489
1800	0.11517	5.01962	0.11027	0.03445
2000	0.02527	4.90878	0.12333	0.03334
2200	0.0038	4.84639	0.13426	0.0323
2400	0.00697	4.73609	0.13535	0.03109
2600	0.00849	4.67675	0.14715	0.0295
2800	0.01473	4.64196	0.16434	0.02746
3000	0.00293	4.50445	0.16798	0.02601
3500	0.00726	4.29793	0.19796	0.02156
4000	0.0217	4.07991	0.23003	0.01741
4500	0.01884	3.85089	0.26488	0.01365
5000	7.70E-04	3.56714	0.29313	0.01067

Table S6. Summary of the fitting parameters of the temperature-dependence of the magnetization relaxation times (τ) for **1**.

Mechanism	Parameter	0 Oe	500 Oe
Orbach	U_{eff}	136.8 K	138.2 K
	τ_0^{-1}	1.02 x 10^{-9} s	1.01 x 10^{-9} s
Raman	C	2.67 x 10^{-3} s^{-1} K^{-n}	1.11 x 10^{-3} s^{-1} K^{-n}
	n	5.97	6.21
QTM	B_1	5 s^{-1}	-
	B_2	-	-

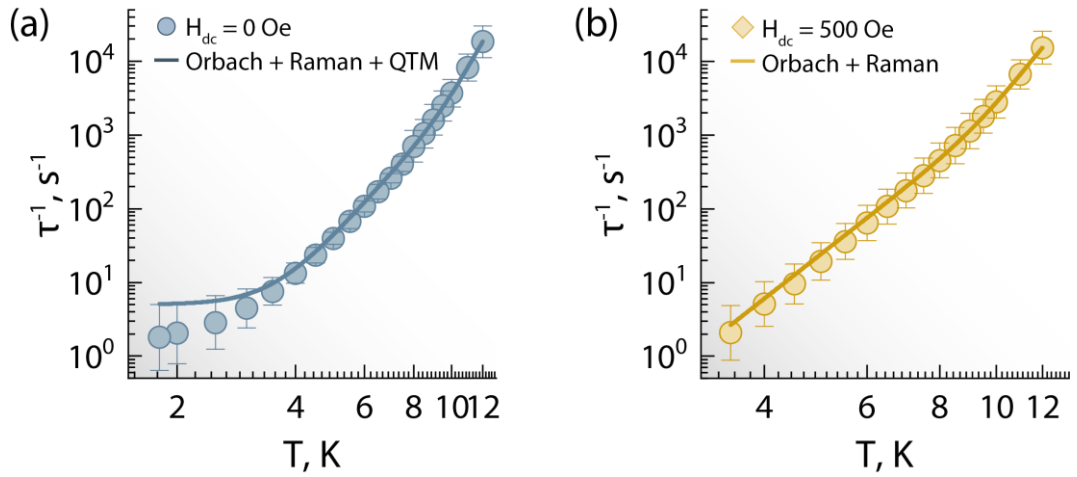

Figure S6. Temperature dependence of the relaxation times of the magnetization (τ^{-1}) in the absence (a) and presence (b, 500 Oe) of a magnetic field with the respective estimated standard deviations for the relaxation processes. The estimated standard deviations of the relaxation time (vertical solid bars) have been calculated from the α-parameters of the generalized Debye fits and the log-normal distribution as described in reference [2].

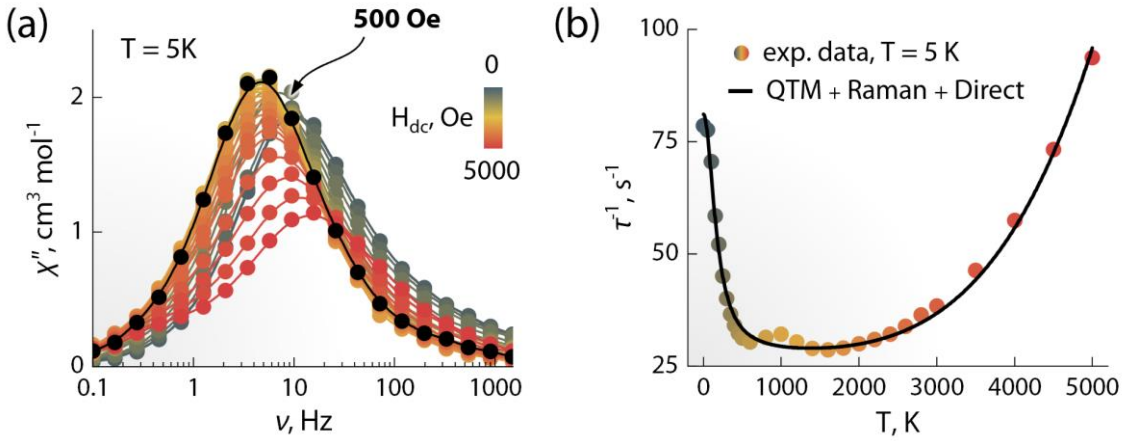

Figure S7. a) Frequency dependence of the out-of-phase (χ'') magnetic susceptibility obtained at 5 K as a function of the applied field. Highlighted in black is the dataset obtained at 500 Oe. **b)** Field dependence of the magnetic relaxation times (τ) measured at 5 K. Black solid line is the best fit to the experimental data using eq. 2 in the main manuscript. Best-fit parameters are summarized in **Table S7**.

Table S7. Summary of the fitting parameters of the field-dependence of the magnetization relaxation times (τ) for **1** obtained at 5 K.

Mechanism	Parameter	5 K
Direct	A	2.17×10^{-14} s^{-1} Oe^{-4} K^{-1}
Raman	C	1.87×10^{-3} s^{-1} K^{-n}
	n	5.97
QTM	B_1	53.30 s^{-1}
	B_2	3.39×10^{-5} T^{-2}

4. Mathematical treatment of luminescence thermometry data

The proposed thermometric approach is a so-called ratiometric method, wherein the thermometric parameter (Δ) is the ratio between the integrated intensity of the luminescence over conveniently defined wavelength ranges. In this study, the integrated signals were obtained over the ranges 571.3-572.1 nm (I_1) and 567.2-570.3 nm (I_2), and $\Delta = I_2/I_1$.

The experimental dataset was fit to a parabolic function of the type $\Delta(T) = \mathbf{A} + \mathbf{B}\cdot T + \mathbf{C}\cdot T^2$ obtaining the values reported in **Table S8** for the three parameters **A**, **B**, and **C**.

Table S8. Summary of parabolic fit parameters of the experimentally obtained calibration curve.

Parameter	Value (error on the last digit)
A	0.443(5)
B	0.0017(4)
C	0.000055(7)
R^2	0.998

This parabolic function Δ(T) was used to determine the relative thermal sensitivity as described in Equation 3 in the main manuscript, which we report here below:

$$S_r = \frac{1}{\Delta(T)}\frac{\partial\Delta(T)}{\partial T} \quad \text{(S1)}$$

The relative thermal sensitivity was then employed to retrieve the temperature uncertainty δT(T). Following the guidelines provided by Brites et al.,[3] we first calculated the uncertainty over the determination of Δ (δΔ) considering the fluctuations of the recorded spectra (δI) in the 555-560 nm range (where no Dy^{3+} emission is observed). A standard deviation of approximately 0.001 was observed in all cases for the normalized spectra, which was considered as δI. In the case of a ratiometric approach, one could consider that:

$$\frac{\delta\Delta}{\Delta} = \sqrt{\left(\frac{\delta I_1}{I_1}\right)^2 + \left(\frac{\delta I_2}{I_2}\right)^2} = \sqrt{2}\frac{\delta I}{I} \quad \text{(S2)}$$

Where the leftmost approximation assumes that the relative uncertainties for I_1 and I_2 are similar. In this case, δI/I is 0.001, since it is obtained by dividing δI by the maximum intensity value (i.e., 1 for the normalized spectra). Finally, since the temperature readout uncertainty is a function of the uncertainty over the thermometric parameter:

$$\delta T(T) = \frac{1}{S_r(T)}\frac{\delta\Delta}{\Delta} \quad \text{(S3)}$$

Combining Equations S2 and S3, δT(T) can be calculated as:

$$\delta T(T) = \frac{1}{S_r(T)}\sqrt{2}\frac{\delta I}{I} \quad \text{(S4)}$$

Which returns the continuous function shown as a grey line in **Figure 4c** of the main manuscript.

The repeatability (R) of the thermometric approach was calculated considering the results of three independent sets of measurements at 10 and 50 K, and using the equation:

$$R = 1 - \frac{\max(|\Delta_i - \Delta_c|)}{\Delta_c} \quad \text{(S5)}$$

Where Δ_i is the thermometric parameter obtained for the i-th measurement and Δ_c is the thermal parameter extracted from the calibration curve. The values for the determination of the repeatability are reported in **Table S9**.

Table S9. Values of the thermometric parameter Δ obtained at 10 and 50 K from the three cycles, and from the calibration curve.

	T	Δ
Cycle 1	10 K	0.468
	50 K	0.662
Cycle 2	10 K	0.471
	50 K	0.664
Cycle 3	10 K	0.469
	50 K	0.668
Calibration	10 K	0.466
	50 K	0.666

5. Computational details, data, and additional discussion

All density function theory (DFT) calculations were performed with Gaussian16.[3] The starting geometries for the model systems $\mathbf{1_O}$, $\mathbf{1_S}$, $\mathbf{1_{Se}}$, and $\mathbf{1_{Te}}$ were constructed from the crystal structure of **1** by replacing sulfur atoms with oxygen ($\mathbf{1_O}$), selenium ($\mathbf{1_{Se}}$), tellurium ($\mathbf{1_{Te}}$) or without any modification ($\mathbf{1_S}$). A full geometry optimization in the gas-phase was carried out for all model systems ($\mathbf{1_O}$, $\mathbf{1_S}$, $\mathbf{1_{Se}}$, and $\mathbf{1_{Te}}$) using the PBE1PBE exchange-correlation functional[4,5] in combination with Grimme's dispersion correction (D3)[6] with Becke-Johson damping factor,[7] whereas for **1** only a partial geometry optimization was performed using the same computational method. In the partial geometry optimization, only the positions of hydrogen atoms of **1** were optimized while all other atoms were frozen to their corresponding crystal structure coordinates. The comparison of results obtained for **1** and $\mathbf{1_S}$ helps to understand the influence of gas-phase optimization on the geometries and microscopic magnetic properties of model systems. As shown below the geometries and magnetic properties of $\mathbf{1_S}$ (gas-phase) and **1** (crystal structure) are not identical but very similar (**Table S10**, **S14**, **S17**, **S19**, **S22**, and **S23** as well as **Figure S7** and **S8**). The similar results obtained for $\mathbf{1_S}$ and **1** underpin the reliability of the computational results calculated for $\mathbf{1_O}$, $\mathbf{1_{Se}}$, and $\mathbf{1_{Te}}$ for which no solid-state structures exist yet. The geometry of $\mathbf{1_S}$ was also optimized without the dispersion correction to investigate the effect of dispersion force on the geometry of $\mathbf{1_S}$. Because the geometry optimizations without and with the dispersion correction gave similar geometries for $\mathbf{1_s}$ (**Table S10**), no geometries of other model systems were optimized without the dispersion correction. In the DFT calculations, triple-zeta valence plus polarization (TZVP) basis sets were used for all atoms,[8,9] except for Dy, for which the polarized double-zeta valence quality was applied.[10] The core electrons of Dy atom were described with the relativistic effective core potential developed by Cundari and Stevens. The subsequent single point energy calculations were done for the optimized structures using the PBE1PBE-D3 exchange-correlation functional in conjunction with all electron basis sets for all atoms.[11] In the single point energy calculations, the scalar relativistic effects were treated using the Douglas-Kroll-Hess Hamiltonian as implemented in Gaussian 16.

The quantum theory of atoms in molecules (QTAIM) analyses were performed for **1**, $\mathbf{1_O}$, $\mathbf{1_S}$, $\mathbf{1_{Se}}$, and $\mathbf{1_{Te}}$ using the electron densities obtained from the single point energy calculations described above.[12] AIMALL software package was used for the QTAIM analyses.[13] The QTAIM analysis is based on the topology of the total electron density of a molecular system, and it provides a way for analyzing and classifying the nature of chemical bonds and interactions in the molecular system.[12] In the QTAIM, the molecular system is partitioned into set of atomic basins. The basins are defined by a surface satisfying the zero-flux condition; the dot product of the gradient of the electron density, $\rho(\mathbf{r})$, and a unit vector, $\mathbf{n}(\mathbf{r})$, normal to the surface at the given point must equal to zero. The points where the gradient of the electron density, $\nabla\rho(\mathbf{r})$, vanishes are called the critical points. They can be classified into the nuclear, bond, ring or cage critical points depending on their character. Among them, the bond critical point is the most useful in quantifying bond character and interactions in the molecular system. It has been proven that when $\rho(\mathbf{r}) > 0.2$ a.u. and $\nabla^2\rho(\mathbf{r}) < 0$ at the bond critical point, the interaction can be interpret as a covalent interaction, whereas $\rho(\mathbf{r}) < 0.1$ a.u. with $\nabla^2\rho(\mathbf{r}) > 0$ represents an ionic, van der Waals, or hydrogen bonding interaction.[14] According to this rule, Dy-O, Dy-N, and Dy-E (E = O, S, Se, Te) bonds can be classified as ionic bonds (**Table S23**). Further inspection of the data reveals that the ionic character of Dy-E bonds decreases when descending the chalcogen group due to the more diffuse nature of frontier orbitals of heavier chalcogen atoms. This is also proven by the calculated delocalization indexes (DI) that measures the degree of electron-sharing between two atoms (**Table S23**).[12]

To evaluate the energies of the first excited singlet and triplet states of coordinated ligands $C_6H_5COO^-$ (ba^-) $C_6H_5COS^-$ (tba^-), $C_6H_5COSe^-$ ($seba^-$), $C_6H_5COTe^-$ ($teba^-$) and phen, time-dependent density functional theory (TD-DFT) calculations were performed for ligands at the CAM-B3LYP[15] and LC-ωPBE[16-18] level of theories along with three different basis sets, namely TZVP[8,9] (only for tba^-), Def2-TZVPP and Def2-QZVPPD, to evaluate the basis set dependence on the energy of the calculated states.[19] Because the results obtained

for tba^- with TZVP and Def2-TZVPP basis sets were similar (**Table S24**), no TZVP basis set was used with any other ligands. Prior to the TD-DFT calculations, the geometries of ligands were optimized to their ground states using the same exchange-correlation functionals and Def2-TZVPP basis set. Electronic transitions to the singlet and triplet states were treated as vertical excitations from the ground state.

The complete active space self-consistent field (CASSCF)[20-22] approach in combination with the restricted active space state interaction (RASSI)[23-25] method was employed to calculate the energies of the spin-orbit states for **1**, $\mathbf{1_O}$, $\mathbf{1_S}$, $\mathbf{1_{Se}}$, and $\mathbf{1_{Te}}$. OpenMolcas (version 19.11) was used to perform all CASSCF/RASSI calculations.[26] In CASSCF/RASSI calculations, the relativistic contracted natural atomic orbital (ANO-RCC) basis set with the polarized triple-zeta valence quality (ANO-RCC-TZVP) and polarized double-zeta valence quality (ANO-RCC-TZVP) were applied for Dy and all other atoms, respectively.[27,28] In state-averaged CASSCF calculations, all sextet, quartet and doublet states of Dy(III) ion generated by nine electrons in seven orbitals were solved. In the subsequent RASSI calculations, the 21 sextets, 128 quartets and 130 doublets were mixed by the spin-orbit coupling. Cholesky decomposition with a threshold value of 10^{-8} was used to reduce the computational time, whereas the relativistic effect was treated using the exact two component (X2C) transformation.[29-31] The **g**-tensors, crystal field parameters and qualitative energy barrier for **1**, $\mathbf{1_O}$, $\mathbf{1_S}$, $\mathbf{1_{Se}}$, and $\mathbf{1_{Te}}$ were extracted from the CASSCF/RASSI wavefunctions utilizing the SINGLE_ANISO program package.[32-34] The effective charges of coordinating atoms were calculated with the LoProp program.[35]

Although the CASSCF/RASSI level of theory predicted the splitting of the ground multiplet $^6H_{15/2}$ well for 1, the calculated splitting and absolute values of the excited multiplets $^6H_{13/2}$ and $^4F_{9/2}$ deviated from the experimental results (**Table S12**, **Figure S9** and **S10**). This is a well-known problem of the CASSCF method and because of this, we only analyzed the general trends not absolute values in the thermometric performance simulations.

Table S10. Selected bond lengths (Å) and angles (°) for the crystal structure and gas-phase optimized structure of **1$_S$** at the PBE1PBE-D3/TZVP[a] and PBE1PBE/TZVP[b] levels of theory and their difference (Exp-Cal) with mean absolute errors (MAE).

Bond	Crys. Struct.	1$_S$[a]	Exp-Cal[a]	1$_S$[b]	Exp-Cal[b]
C1 – Dy1	2.906	2.960	0.054	2.960	0.054
C8 – Dy1	2.937	2.935	0.002	2.955	0.018
C15 – Dy1	2.910	2.956	0.046	2.960	0.050
N1 – Dy1	2.478	2.526	0.048	2.543	0.065
N2 – Dy1	2.525	2.550	0.025	2.571	0.046
O1 – Dy1	2.342	2.385	0.043	2.371	0.029
O2 – Dy1	2.341	2.361	0.020	2.383	0.042
O3 – Dy1	2.371	2.377	0.006	2.372	0.001
S1 – Dy1	2.796	2.845	0.049	2.858	0.062
S2 – Dy1	2.836	2.817	0.019	2.833	0.003
S3 – Dy1	2.818	2.846	0.029	2.858	0.041
MAE			0.031		0.037
Angle	**Crys. Struct.**	**1$_S$[a]**	**Exp-Cal[a]**	**1$_S$[b]**	**Exp-Cal[b]**
C26 – N1 – Dy1	119.90	119.76	0.14	120.01	0.11
C30 – N2 – Dy1	118.40	118.76	0.36	118.88	0.48
C1 – O1 – Dy1	103.60	104.48	0.88	105.16	1.56
C8 – O2 – Dy1	105.10	104.05	1.05	104.12	0.98
C15 – O3 – Dy1	102.10	104.73	2.63	105.13	3.03
C1 – S1 – Dy1	76.11	76.41	0.30	76.03	0.08
C8 – S2 – Dy1	76.13	76.44	0.31	76.67	0.54
C15 – S3 – Dy1	75.75	76.23	0.48	76.06	0.31
N1 – Dy1 – N2	65.58	64.73	0.85	64.29	1.29
N1 – Dy1 – S1	91.50	82.30	9.20	85.57	5.93
N1 – Dy1 – S2	157.81	158.91	1.10	160.21	2.40
N1 – Dy1 – S3	92.78	83.10	9.68	84.19	8.59
N2 – Dy1 – S1	85.57	78.74	6.83	79.13	6.44
N2 – Dy1 – S2	136.50	136.35	0.15	135.49	1.01
N2 – Dy1 – S3	84.97	78.05	6.92	79.44	5.53
O1 – Dy1 – N1	79.07	75.94	3.13	76.94	2.13
O1 – Dy1 – N2	129.41	125.12	4.29	124.21	5.20
O1 – Dy1 – O3	74.78	76.98	2.20	78.68	3.90
O1 – Dy1 – S1	59.45	58.71	0.74	58.56	0.89
O1 – Dy1 – S2	82.03	87.35	5.32	88.06	6.03
O1 – Dy1 – S3	133.55	134.48	0.93	136.16	2.61
O2 – Dy1 – N1	143.19	141.75	1.44	140.89	2.30
O2 – Dy1 – N2	77.69	77.06	0.63	76.62	1.07
O2 – Dy1 – O1	126.44	129.50	3.06	130.59	4.15
O2 – Dy1 – O3	128.14	131.85	3.71	129.03	0.89
O2 – Dy1 – S1	82.97	88.88	5.91	88.38	5.41
O2 – Dy1 – S2	58.81	59.31	0.50	58.88	0.07
O2 – Dy1 – S3	86.22	91.04	4.82	87.75	1.53
O3 – Dy1 – N1	80.44	75.84	4.60	77.28	3.16
O3 – Dy1 – N2	128.90	124.17	4.73	125.35	3.55
O3 – Dy1 – S1	134.21	134.19	0.02	136.59	2.38
O3 – Dy1 – S2	83.48	88.07	4.59	87.27	3.79
O3 – Dy1 – S3	58.77	58.73	0.04	58.56	0.21
S1 – Dy1 – S2	88.82	100.10	11.28	97.66	8.84
S1 – Dy1 – S3	166.93	156.19	10.74	158.54	8.39
S3 – Dy1 – S2	91.85	100.30	8.45	98.35	6.50
MAE			**3.39**		**3.09**

Table S11. Selected bond lengths (Å) and angles (°) for $\mathbf{1_O}$, $\mathbf{1_{se}}$, and $\mathbf{1_{Te}}$ at the PBE1PBE-D3/TZV level of theory.

Bond length	$\mathbf{1_O}$	$\mathbf{1_{se}}$	$\mathbf{1_{Te}}$
C1 – Dy1 (C1 – Dy 65)	2.747	3.014	3.087
C8 – Dy1 (C13 – Dy65)	2.741	2.994	3.064
C15 – Dy1 (C25 – Dy65)	2.747	3.015	3.083
N1 – Dy1 (N57 – Dy65)	2.450	2.514	2.517
N2 – Dy1 (N58 – Dy65)	2.550	2.561	2.552
O1 – Dy1 (O59 – Dy65)	2.384	2.399	2.383
O2 – Dy1 (O60 – Dy65)	2.389	2.373	2.366
O3 – Dy1 (O61 – Dy65)	2.385	2.402	2.385
E1 – Dy1 (E62 – Dy65)	2.395	2.954	3.187
E2 – Dy1 (E63 – Dy65)	2.370	2.941	3.164
E3 – Dy1 (E64 – Dy65)	2.392	2.952	3.176
Angle			
N1 – Dy1 – N2 (N57 – Dy65 – N58)	64.51	64.83	64.91
N1 – Dy1 – E1 (N57 – Dy65 – E62)	80.98	83.81	83.82
N1 – Dy1 – E2 (N57 – Dy65 – E63)	163.18	158.40	157.61
N1 – Dy1 – E3 (N57 – Dy65 – E64)	80.28	84.05	85.90
N2 – Dy1 – E1 (N58 – Dy65 – E62)	78.04	78.60	79.54
N2 – Dy1 – E2 (N58 – Dy65 – E63)	132.15	136.77	137.44
N2 – Dy1 – E3 (N58 – Dy65 – E64)	77.13	78.57	78.23
O1 – Dy1 – N1 (O59 – Dy65 – N57)	76.34	75.81	76.38
O1 – Dy1 – N2 (O59 – Dy65 – N58)	122.52	125.15	127.00
O1 – Dy1 – O3 (O59 – Dy65 – O61)	83.81	75.75	74.30
O1 – Dy1 – E1 (O59 – Dy65 – E62)	54.79	59.93	60.93
O1 – Dy1 – E2 (O59 – Dy65 – E63)	89.92	87.32	86.24
O1 – Dy1 – S3 (O59 – Dy65 – E64)	136.41	134.67	134.92
O2 – Dy1 – N1 (O60 – Dy65 – N57)	141.73	141.30	140.84
O2 – Dy1 – N2 (O60 – Dy65 – N58)	77.24	76.47	76.10
O2 – Dy1 – O1 (O60 – Dy65 – O59)	127.64	131.15	129.20
O2 – Dy1 – O3 (O60 – Dy65 – O61)	129.77	131.63	134.39
O2 – Dy1 – E1 (O60 – Dy65 – E62)	90.47	88.55	85.80
O2 – Dy1 – E2 (O60 – Dy65 – E63)	54.93	60.30	61.52
O2 – Dy1 – E3 (O60 – Dy65 – E64)	92.79	88.80	89.83
O3 – Dy1 – N1 (O61 – Dy65 – N57)	75.75	75.65	75.59
O3 – Dy1 – N2 (O61 – Dy65 – N58)	121.74	124.90	124.60
O3 – Dy1 – S1 (O61 – Dy65 – E62)	136.35	134.54	134.00
O3 – Dy1 – S2 (O61 – Dy65 – E63)	93.38	87.30	86.29
O3 – Dy1 – S3 (O61 – Dy65 – E64)	54.80	59.94	61.14
E1 – Dy1 – E2 (E62 – Dy65 – E63)	99.16	99.49	100.11
E1 – Dy1 – E3 (E62 – Dy65 – E64)	153.57	157.01	157.75
E3 – Dy1 – E2 (E64 – Dy65 – E63)	104.15	98.98	96.90

Table S12. Calculated energies (*E*) for each KD arising from the crystal-field splitting of ground $^6H_{15/2}$ and excited $^6H_{13/2}$ and $^4F_{9/2}$ multiplets of **1** as well as the eigenvalues of ***g***-tensors for each KD arising from the crystal-field splitting of ground $^6H_{15/2}$ multiplet and angle (Θ) between the ground KD and excited KD at the CASSCF/RASSI[a] level.

		$^6H_{15/2}$			
KD	***E*** **[cm^{-1}][a]**	g_x	g_y	g_z	Θ **[°]**
1	0.000	0.001	0.001	19.832	-
2	107.555	0.025	0.036	17.829	24.186
3	167.494	1.127	1.703	14.000	5.524
4	212.741	1.395	3.047	11.023	14.929
5	257.954	0.051	3.977	10.426	37.320
6	289.580	3.245	6.371	11.909	80.625
7	436.649	0.887	2.968	14.459	92.123
8	469.414	0.548	3.891	15.847	93.416
		$^6H_{13/2}$			
KD	***E*** **[cm^{-1}][a]**	g_x	g_y	g_z	Θ **[°]**
1	3576.434	-	-	-	-
2	3642.338	-	-	-	-
3	3723.961	-	-	-	-
4	3799.689	-	-	-	-
5	3844.296	-	-	-	-
6	3878.530	-	-	-	-
7	3899.563	-	-	-	-
		$^4F_{9/2}$			
KD	***E*** **[cm^{-1}][a]**	g_x	g_y	g_z	Θ **[°]**
1	24573.046	-	-	-	-
2	24655.711	-	-	-	-
3	24676.906	-	-	-	-
4	24759.694	-	-	-	-
5	24787.026	-	-	-	-

Table S13. Calculated energies (*E*) for each KD arising from the crystal-field splitting of ground $^6H_{15/2}$ and excited $^6H_{13/2}$ and $^4F_{9/2}$ multiplets of $\mathbf{1_O}$ as well as the eigenvalues of ***g***-tensors for each KD arising from the crystal-field splitting of ground $^6H_{15/2}$ multiplet and angle (Θ) between the ground KD and excited KD at the CASSCF/RASSI[a] level.

		$^6H_{15/2}$			
KD	***E*** **[cm^{-1}][a]**	$\mathbf{g_x}$	$\mathbf{g_y}$	$\mathbf{g_z}$	**Θ [°]**
1	0.000	0.803	4.906	15.126	-
2	32.437	1.139	2.774	11.402	85.732
3	78.240	1.725	5.799	11.708	102.611
4	98.400	0.384	2.189	15.060	67.536
5	133.220	1.319	4.249	10.746	107.079
6	200.515	1.072	3.019	14.009	92.309
7	225.164	0.439	1.807	17.410	131.399
8	291.843	0.270	0.405	19.298	49.073
		$^6H_{13/2}$			
KD	***E*** **[cm^{-1}]**	$\mathbf{g_x}$	$\mathbf{g_y}$	$\mathbf{g_z}$	**Θ [°]**
1	3582.440	-	-	-	-
2	3611.957	-	-	-	-
3	3637.386	-	-	-	-
4	3654.396	-	-	-	-
5	3675.603	-	-	-	-
6	3699.270	-	-	-	-
7	3746.220	-	-	-	-
		$^4F_{9/2}$			
KD	***E*** **[cm^{-1}]**	$\mathbf{g_x}$	$\mathbf{g_y}$	$\mathbf{g_z}$	**Θ [°]**
1	24462.938	-	-	-	-
2	24546.424	-	-	-	-
3	24595.923	-	-	-	-
4	24659.027	-	-	-	-
5	24722.841	-	-	-	-

Table S14. Calculated energies (*E*) for each KD arising from the crystal-field splitting of ground $^6H_{15/2}$ and excited $^6H_{13/2}$ and $^4F_{9/2}$ multiplets of $\mathbf{1_S}$ as well as the eigenvalues of ***g***-tensors for each KD arising from the crystal-field splitting of ground $^6H_{15/2}$ multiplet and angle (Θ) between the ground KD and excited KD at the CASSCF/RASSI[a] level.

		$^6H_{15/2}$			
KD	***E*** **[cm^{-1}][a]**	$\mathbf{g_x}$	$\mathbf{g_y}$	$\mathbf{g_z}$	**Θ [°]**
1	0.000	0.003	0.004	19.767	-
2	103.187	0.199	0.220	17.443	20.334
3	147.517	1.993	2.896	12.819	4.630
4	182.589	1.189	2.575	11.437	26.282
5	200.935	0.616	3.084	14.496	53.728
6	232.358	3.266	6.470	10.822	94.314
7	376.476	1.060	3.938	13.316	92.142
8	404.660	0.648	5.028	14.880	89.925
		$^6H_{13/2}$			
KD	***E*** **[cm^{-1}]**	$\mathbf{g_x}$	$\mathbf{g_y}$	$\mathbf{g_z}$	**Θ [°]**
1	3576.265	-	-	-	-
2	3625.209	-	-	-	-
3	3693.058	-	-	-	-
4	3756.239	-	-	-	-
5	3797.537	-	-	-	-
6	3827.499	-	-	-	-
7	3839.980	-	-	-	-
		$^4F_{9/2}$			
KD	***E*** **[cm^{-1}]**	$\mathbf{g_x}$	$\mathbf{g_y}$	$\mathbf{g_z}$	**Θ [°]**
1	24557.522	-	-	-	-
2	24628.609	-	-	-	-
3	24661.553	-	-	-	-
4	24731.931	-	-	-	-
5	24755.892	-	-	-	-

Table S15. Calculated energies (*E*) for each KD arising from the crystal-field splitting of ground $^6H_{15/2}$ and excited $^6H_{13/2}$ and $^4F_{9/2}$ multiplets of $\mathbf{1_{Se}}$ as well as the eigenvalues of ***g***-tensors for each KD arising from the crystal-field splitting of ground $^6H_{15/2}$ multiplet and angle (Θ) between the ground KD and excited KD at the CASSCF/RASSI[a] level.

		$^6H_{15/2}$			
KD	***E*** **[cm^{-1}][a]**	$\mathbf{g_x}$	$\mathbf{g_y}$	$\mathbf{g_z}$	**Θ [°]**
1	0.000	0.004	0.004	19.751	-
2	95.055	0.155	0.164	17.501	20.210
3	148.454	1.821	2.149	13.436	1.990
4	185.565	0.068	3.192	11.637	24.308
5	200.314	0.683	5.182	11.663	59.077
6	238.384	3.026	5.122	11.963	90.020
7	376.932	0.939	2.604	14.100	90.348
8	407.491	0.544	3.566	15.851	90.405
		$^6H_{13/2}$			
KD	***E*** **[cm^{-1}]**	$\mathbf{g_x}$	$\mathbf{g_y}$	$\mathbf{g_z}$	**Θ [°]**
1	3573.054	-	-	-	-
2	3625.236	-	-	-	-
3	3691.232	-	-	-	-
4	3752.531	-	-	-	-
5	3797.634	-	-	-	-
6	3830.680	-	-	-	-
7	3849.368	-	-	-	-
		$^4F_{9/2}$			
KD	***E*** **[cm^{-1}]**	$\mathbf{g_x}$	$\mathbf{g_y}$	$\mathbf{g_z}$	**Θ [°]**
1	24569.308	-	-	-	-
2	24635.951	-	-	-	-
3	24665.960	-	-	-	-
4	24727.506	-	-	-	-
5	24758.574	-	-	-	-

Table S16. Calculated energies (*E*) for each KD arising from the crystal-field splitting of ground $^6H_{15/2}$ and excited $^6H_{13/2}$ and $^4F_{9/2}$ multiplets of $\mathbf{1_{Te}}$ as well as the eigenvalues of ***g***-tensors for each KD arising from the crystal-field splitting of ground $^6H_{15/2}$ multiplet and angle (Θ) between the ground KD and excited KD at the CASSCF/RASSI[a] level.

		$^6H_{15/2}$			
KD	***E*** **[cm^{-1}][a]**	$\mathbf{g_x}$	$\mathbf{g_y}$	$\mathbf{g_z}$	$\boldsymbol{\Theta}$ **[°]**
1	0.000	0.002	0.003	19.806	-
2	111.046	0.048	0.054	17.360	15.267
3	183.950	0.444	0.472	14.451	2.832
4	234.374	1.065	1.833	13.567	32.523
5	275.454	2.730	5.584	8.713	42.537
6	337.959	2.894	4.135	12.313	89.383
7	482.228	0.608	0.876	15.056	90.080
8	532.045	0.351	1.605	17.329	92.709
		$^6H_{13/2}$			
KD	***E*** **[cm^{-1}]**	$\mathbf{g_x}$	$\mathbf{g_y}$	$\mathbf{g_z}$	$\boldsymbol{\Theta}$ **[°]**
1	3582.386	-	-	-	-
2	3647.969	-	-	-	-
3	3740.148	-	-	-	-
4	3820.077	-	-	-	-
5	3876.499	-	-	-	-
6	3923.474	-	-	-	-
7	3970.047	-	-	-	-
		$^4F_{9/2}$			
KD	***E*** **[cm^{-1}]**	$\mathbf{g_x}$	$\mathbf{g_y}$	$\mathbf{g_z}$	$\boldsymbol{\Theta}$ **[°]**
1	24637.131	-	-	-	-
2	24699.535	-	-	-	-
3	24726.672	-	-	-	-
4	24777.329	-	-	-	-
5	24835.852	-	-	-	-

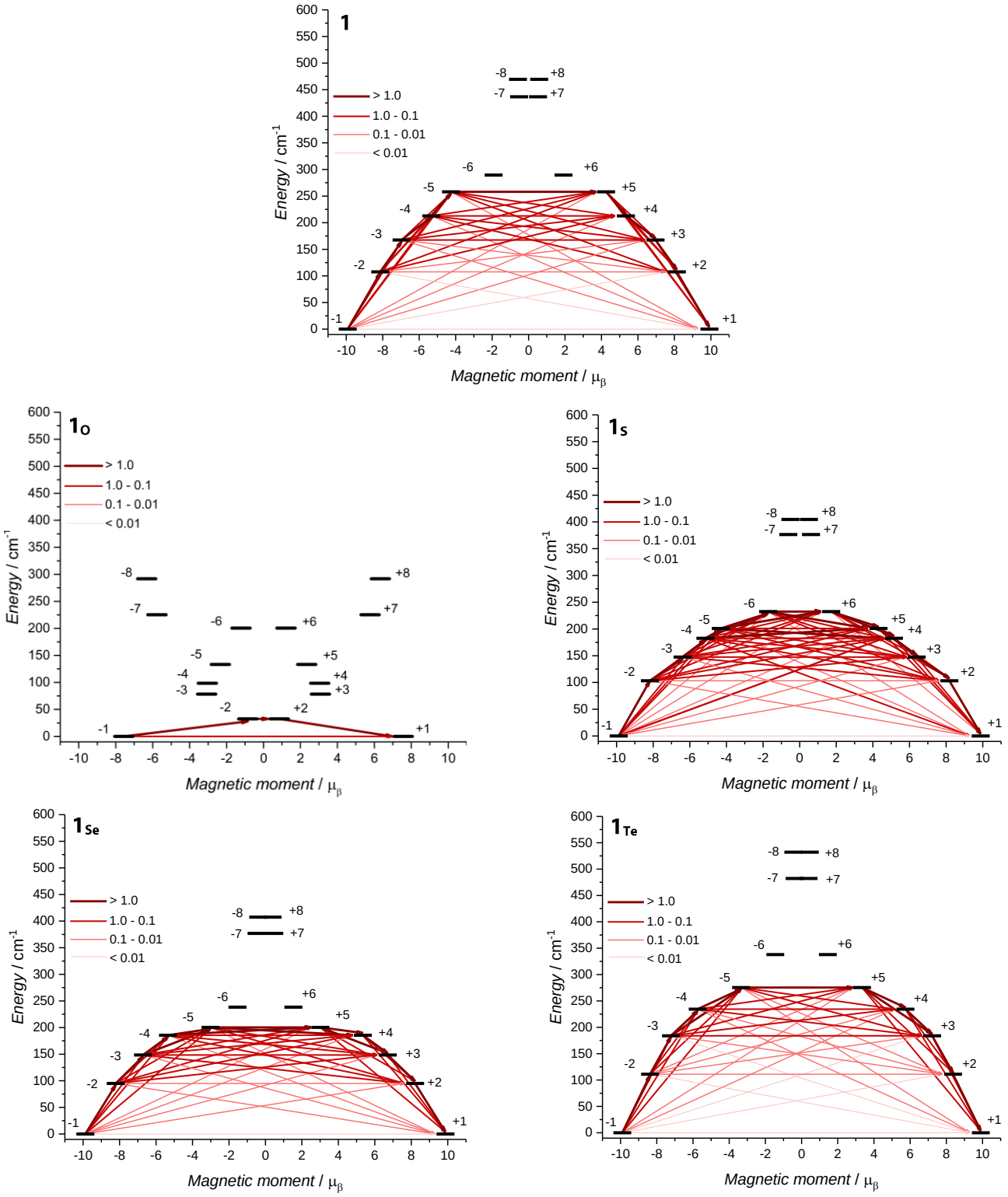

Figure S8. Calculated qualitative energy barriers for **1**, **1**$_O$, **1**$_S$, **1**$_{Se}$, and **1**$_{Te}$. The values of transition magnetic moment matrix elements, that is, the transition probabilities between the different spin-orbit states, are presented with the different shades of red.

Table S17. Calculated crystal-field parameters B_{kq} (cm^{-1}) presented in Iwahara-Chibotaru notation for **1**.

k	q	Re|B_{kq}|	Im|B_{kq}|	|B_{kq}|
2	0	-244.2294	0.0000	244.2290
2	1	10.2675	-9.1864	13.7770
2	2	6.0743	9.9206	11.6330
4	0	25.3116	0.0000	25.3120
4	1	11.2394	-5.0321	12.3140
4	2	4.3955	-1.0779	4.5260
4	3	-1.6423	-21.3590	21.4220
4	4	31.8409	39.1069	50.4300
6	0	-22.7671	0.0000	22.7670
6	1	-13.2668	7.7268	15.3530
6	2	-4.7267	5.5182	7.2660
6	3	1.8872	4.4409	4.8250
6	4	-6.0812	-7.6553	9.7770
6	5	0.0379	0.2201	0.2230
6	6	-3.6729	1.1822	3.8580
8	0	0.2528	0.0000	0.2530
8	1	0.2062	-0.1050	0.2310
8	2	0.0195	0.0491	0.0530
8	3	-0.0562	-0.2934	0.2990
8	4	0.1669	0.1772	0.2430
8	5	-0.0444	-0.0200	0.0490
8	6	0.0324	-0.0112	0.0340
8	7	-0.0037	-0.0011	0.0040
8	8	-0.0054	0.0225	0.0230
10	0	0.0195	0.0000	0.0200
10	1	-0.0198	0.0184	0.0270
10	2	-0.0035	-0.0091	0.0100
10	3	0.0074	0.0379	0.0390
10	4	-0.0146	-0.0117	0.0190
10	5	0.0166	0.0066	0.0180
10	6	0.0019	-0.0017	0.0020
10	7	-0.0033	0.0040	0.0050
10	8	0.0025	-0.0100	0.0100
10	9	0.0000	0.0012	0.0010
10	10	-0.0050	-0.0033	0.0060
12	0	-0.0019	0.0000	0.0020
12	1	0.0011	-0.0013	0.0020
12	2	0.0008	-0.0003	0.0010
12	3	-0.0004	-0.0021	0.0020
12	4	0.0008	0.0006	0.0010
12	5	-0.0007	-0.0003	0.0010
12	6	0.0001	0.0000	0.0000
12	7	0.0000	0.0000	0.0000
12	8	-0.0001	0.0003	0.0000
12	9	0.0000	0.0000	0.0000
12	10	0.0001	0.0001	0.0000
12	11	0.0000	0.0000	0.0000
12	12	0.0001	0.0000	0.0000

14	0	0.0000	0.0000	0.0000
14	1	0.0000	0.0000	0.0000
14	2	0.0000	0.0000	0.0000
14	3	0.0000	0.0000	0.0000
14	4	0.0000	0.0000	0.0000
14	5	0.0000	0.0000	0.0000
14	6	0.0000	0.0000	0.0000
14	7	0.0000	0.0000	0.0000
14	8	0.0000	0.0000	0.0000
14	9	0.0000	0.0000	0.0000
14	10	0.0000	0.0000	0.0000
14	11	0.0000	0.0000	0.0000
14	12	0.0000	0.0000	0.0000
14	13	0.0000	0.0000	0.0000
14	14	0.0000	0.0000	0.0000

Table S18. Calculated crystal-field parameters B_{kq} (cm^{-1}) presented in Iwahara-Chibotaru notation for $\mathbf{1_O}$.

k	q	Re|B_{kq}|	Im|B_{kq}|	|B_{kq}|
2	0	-13.8411	0.0000	13.8410
2	1	-24.6044	3.2267	24.8150
2	2	49.1785	6.4227	49.5960
4	0	-67.1629	0.0000	67.1630
4	1	12.5641	-3.5619	13.0590
4	2	50.7856	-23.9279	56.1400
4	3	-3.1414	2.0633	3.7580
4	4	-16.8012	-9.5501	19.3260
6	0	1.3563	0.0000	1.3560
6	1	2.6096	1.8857	3.2200
6	2	15.2785	7.0566	16.8290
6	3	-1.7395	1.9004	2.5760
6	4	14.0443	1.8824	14.1700
6	5	1.7906	0.8785	1.9940
6	6	15.6348	-14.8882	21.5890
8	0	0.1532	0.0000	0.1530
8	1	-0.0572	0.0115	0.0580
8	2	-0.2145	-0.0368	0.2180
8	3	0.0263	0.0044	0.0270
8	4	0.0060	0.0337	0.0340
8	5	0.0562	-0.0072	0.0570
8	6	0.1764	-0.0711	0.1900
8	7	-0.0035	0.0041	0.0050
8	8	-0.0080	0.0304	0.0310
10	0	0.0372	0.0000	0.0370
10	1	-0.0202	-0.0006	0.0200
10	2	-0.0190	-0.0119	0.0220
10	3	0.0055	-0.0051	0.0070
10	4	0.0017	-0.0141	0.0140
10	5	-0.0026	0.0056	0.0060
10	6	0.0073	0.0007	0.0070
10	7	0.0041	0.0008	0.0040
10	8	0.0093	-0.0192	0.0210
10	9	-0.0015	0.0023	0.0030
10	10	-0.0097	0.0000	0.0100
12	0	0.0028	0.0000	0.0030
12	1	-0.0007	0.0006	0.0010
12	2	0.0013	-0.0001	0.0010
12	3	-0.0001	0.0003	0.0000
12	4	0.0006	0.0002	0.0010
12	5	-0.0003	0.0002	0.0000
12	6	0.0005	0.0004	0.0010
12	7	-0.0003	0.0001	0.0000
12	8	0.0003	0.0002	0.0000
12	9	0.0001	0.0001	0.0000
12	10	0.0006	-0.0005	0.0010
12	11	0.0002	-0.0001	0.0000
12	12	0.0001	-0.0017	0.0020

14	0	0.0000	0.0000	0.0000
14	1	0.0000	0.0000	0.0000
14	2	0.0000	0.0000	0.0000
14	3	0.0000	0.0000	0.0000
14	4	0.0000	0.0000	0.0000
14	5	0.0000	0.0000	0.0000
14	6	0.0000	0.0000	0.0000
14	7	0.0000	0.0000	0.0000
14	8	0.0000	0.0000	0.0000
14	9	0.0000	0.0000	0.0000
14	10	0.0000	0.0000	0.0000
14	11	0.0000	0.0000	0.0000
14	12	0.0000	0.0000	0.0000
14	13	0.0000	0.0000	0.0000
14	14	0.0000	0.0000	0.0000

Table S19. Calculated crystal-field parameters B_{kq} (cm^{-1}) presented in Iwahara-Chibotaru notation for $\mathbf{1_S}$.

k	q	Re|B_{kq}|	Im|B_{kq}|	|B_{kq}|
2	0	-199.3401	0.0000	199.3400
2	1	3.0213	-0.8594	3.1410
2	2	0.6791	21.6321	21.6430
4	0	17.1286	0.0000	17.1290
4	1	-13.4127	16.8845	21.5640
4	2	2.0854	-10.5261	10.7310
4	3	8.7988	18.8222	20.7770
4	4	40.8010	14.5626	43.3220
6	0	-21.7406	0.0000	21.7410
6	1	8.5657	-11.1041	14.0240
6	2	-0.4965	5.4333	5.4560
6	3	1.1725	1.4743	1.8840
6	4	-11.1736	-3.0457	11.5810
6	5	2.8329	-2.7191	3.9270
6	6	-3.1314	6.1781	6.9260
8	0	0.1763	0.0000	0.1760
8	1	-0.0588	0.0983	0.1150
8	2	-0.0475	0.0408	0.0630
8	3	0.0590	0.1959	0.2050
8	4	0.2025	0.0401	0.2060
8	5	0.0405	-0.0033	0.0410
8	6	0.0093	-0.0353	0.0360
8	7	-0.0057	-0.0192	0.0200
8	8	0.0209	0.0145	0.0250
10	0	0.0322	0.0000	0.0320
10	1	0.0054	-0.0198	0.0210
10	2	0.0077	0.0058	0.0100
10	3	-0.0142	-0.0308	0.0340
10	4	-0.0132	-0.0001	0.0130
10	5	-0.0122	0.0072	0.0140
10	6	-0.0006	-0.0006	0.0010
10	7	0.0009	-0.0010	0.0010
10	8	-0.0068	-0.0052	0.0090
10	9	0.0016	-0.0022	0.0030
10	10	-0.0064	0.0060	0.0090
12	0	-0.0016	0.0000	0.0020
12	1	-0.0003	0.0013	0.0010
12	2	-0.0001	-0.0014	0.0010
12	3	0.0005	0.0012	0.0010
12	4	0.0007	0.0000	0.0010
12	5	0.0005	-0.0002	0.0010
12	6	0.0001	0.0000	0.0000
12	7	-0.0001	-0.0003	0.0000
12	8	0.0003	0.0002	0.0000
12	9	-0.0002	0.0001	0.0000
12	10	0.0001	-0.0002	0.0000
12	11	0.0000	0.0001	0.0000
12	12	-0.0001	-0.0001	0.0000

14	0	0.0000	0.0000	0.0000
14	1	0.0000	0.0000	0.0000
14	2	0.0000	0.0000	0.0000
14	3	0.0000	0.0000	0.0000
14	4	0.0000	0.0000	0.0000
14	5	0.0000	0.0000	0.0000
14	6	0.0000	0.0000	0.0000
14	7	0.0000	0.0000	0.0000
14	8	0.0000	0.0000	0.0000
14	9	0.0000	0.0000	0.0000
14	10	0.0000	0.0000	0.0000
14	11	0.0000	0.0000	0.0000
14	12	0.0000	0.0000	0.0000
14	13	0.0000	0.0000	0.0000
14	14	0.0000	0.0000	0.0000

Table S20. Calculated crystal-field parameters B_{kq} (cm^{-1}) presented in Iwahara-Chibotaru notation for $\mathbf{1_{Se}}$.

k	q	Re|B_{kq}|	Im|B_{kq}|	|B_{kq}|
2	0	-204.4090	0.0000	204.4090
2	1	0.9371	0.6004	1.1130
2	2	-28.1790	-16.1403	32.4740
4	0	18.5831	0.0000	18.5830
4	1	-17.9756	-5.1097	18.6880
4	2	8.5507	3.9219	9.4070
4	3	-14.5309	-14.2678	20.3650
4	4	-20.0704	-33.5352	39.0820
6	0	-18.1855	0.0000	18.1860
6	1	13.2784	3.5883	13.7550
6	2	-5.8059	-3.1893	6.6240
6	3	-0.5088	-0.3935	0.6430
6	4	6.1673	10.3206	12.0230
6	5	-0.7641	-2.8546	2.9550
6	6	0.2083	6.5200	6.5230
8	0	0.1765	0.0000	0.1770
8	1	-0.1108	-0.0343	0.1160
8	2	-0.0343	-0.0176	0.0390
8	3	-0.1210	-0.1207	0.1710
8	4	-0.0903	-0.1745	0.1960
8	5	-0.0103	-0.0288	0.0310
8	6	0.0018	-0.0399	0.0400
8	7	0.0041	-0.0174	0.0180
8	8	-0.0094	0.0169	0.0190
10	0	0.0285	0.0000	0.0280
10	1	0.0127	0.0058	0.0140
10	2	-0.0012	-0.0011	0.0020
10	3	0.0218	0.0222	0.0310
10	4	0.0038	0.0107	0.0110
10	5	0.0039	0.0128	0.0130
10	6	0.0001	-0.0002	0.0000
10	7	0.0004	-0.0017	0.0020
10	8	0.0042	-0.0080	0.0090
10	9	-0.0007	0.0006	0.0010
10	10	0.0060	-0.0039	0.0070
12	0	-0.0016	0.0000	0.0020
12	1	-0.0005	-0.0003	0.0010
12	2	0.0009	0.0006	0.0010
12	3	-0.0011	-0.0011	0.0020
12	4	-0.0002	-0.0006	0.0010
12	5	-0.0002	-0.0006	0.0010
12	6	0.0000	-0.0001	0.0000
12	7	0.0001	-0.0003	0.0000
12	8	-0.0002	0.0003	0.0000
12	9	0.0001	-0.0001	0.0000
12	10	-0.0002	0.0001	0.0000

12	11	0.0001	0.0000	0.0000
12	12	-0.0001	0.0000	0.0000
14	0	0.0000	0.0000	0.0000
14	1	0.0000	0.0000	0.0000
14	2	0.0000	0.0000	0.0000
14	3	0.0000	0.0000	0.0000
14	4	0.0000	0.0000	0.0000
14	5	0.0000	0.0000	0.0000
14	6	0.0000	0.0000	0.0000
14	7	0.0000	0.0000	0.0000
14	8	0.0000	0.0000	0.0000
14	9	0.0000	0.0000	0.0000
14	10	0.0000	0.0000	0.0000
14	11	0.0000	0.0000	0.0000
14	12	0.0000	0.0000	0.0000
14	13	0.0000	0.0000	0.0000
14	14	0.0000	0.0000	0.0000

Table S21. Calculated crystal-field parameters B_{kq} (cm^{-1}) presented in Iwahara-Chibotaru notation for $\mathbf{1_{Te}}$.

k	q	Re|B_{kq}|	Im|B_{kq}|	|B_{kq}|
2	0	-281.8421	0.0000	281.8420
2	1	-3.2354	2.5738	4.1340
2	2	48.5376	-21.1207	52.9340
4	0	32.3338	0.0000	32.3340
4	1	2.9269	-18.6850	18.9130
4	2	-8.0610	9.0493	12.1190
4	3	11.8471	13.9130	18.2740
4	4	-20.7833	26.8215	33.9310
6	0	-18.1336	0.0000	18.1340
6	1	-0.3379	12.7328	12.7370
6	2	4.6570	-2.4129	5.2450
6	3	0.1572	0.1467	0.2150
6	4	9.5454	-10.3921	14.1110
6	5	-1.1912	-2.7990	3.0420
6	6	-1.1289	5.8808	5.9880
8	0	0.2103	0.0000	0.2100
8	1	0.0636	-0.1454	0.1590
8	2	0.0063	-0.0093	0.0110
8	3	0.1341	0.0703	0.1510
8	4	-0.1868	0.1936	0.2690
8	5	-0.0258	0.0162	0.0310
8	6	0.0180	-0.0472	0.0510
8	7	0.0183	0.0004	0.0180
8	8	0.0013	-0.0100	0.0100
10	0	0.0200	0.0000	0.0200
10	1	-0.0141	0.0230	0.0270
10	2	0.0048	0.0012	0.0050
10	3	-0.0209	-0.0189	0.0280
10	4	0.0118	-0.0091	0.0150
10	5	0.0094	0.0064	0.0110
10	6	0.0018	0.0024	0.0030
10	7	0.0031	-0.0003	0.0030
10	8	0.0022	0.0094	0.0100
10	9	0.0013	0.0019	0.0020
10	10	-0.0034	-0.0037	0.0050
12	0	-0.0014	0.0000	0.0010
12	1	0.0007	-0.0010	0.0010
12	2	-0.0008	0.0002	0.0010
12	3	0.0013	0.0011	0.0020
12	4	-0.0006	0.0006	0.0010
12	5	-0.0006	-0.0003	0.0010
12	6	-0.0001	-0.0002	0.0000
12	7	0.0002	0.0000	0.0000
12	8	-0.0001	-0.0005	0.0000
12	9	-0.0002	-0.0001	0.0000
12	10	0.0001	0.0002	0.0000
12	11	0.0001	0.0000	0.0000
12	12	-0.0001	0.0000	0.0000
14	0	0.0000	0.0000	0.0000

14	1	0.0000	0.0000	0.0000
14	2	0.0000	0.0000	0.0000
14	3	0.0000	0.0000	0.0000
14	4	0.0000	0.0000	0.0000
14	5	0.0000	0.0000	0.0000
14	6	0.0000	0.0000	0.0000
14	7	0.0000	0.0000	0.0000
14	8	0.0000	0.0000	0.0000
14	9	0.0000	0.0000	0.0000
14	10	0.0000	0.0000	0.0000
14	11	0.0000	0.0000	0.0000
14	12	0.0000	0.0000	0.0000
14	13	0.0000	0.0000	0.0000
14	14	0.0000	0.0000	0.0000

Table S22. Calculated LoProp and AIM charges for the selected atoms of **1**, **1**$_O$, **1**$_S$, **1**$_{Se}$, and **1**$_{Te}$.

	1		**1**$_O$		**1**$_S$		**1**$_{Se}$		**1**$_{Te}$	
Atom	**LoProp**	**AIM**	**LoProp**	**AIM**	**LoProp**	**AIM**	**LoProp**	**AIM**	**LoProp**	**AIM**
N57	-0.39	-1.21	-0.37	-0.39	-1.21	-0.37	-0.39	-1.21	-0.37	-0.39
N58	-0.38	-1.21	-0.36	-0.38	-1.21	-0.36	-0.38	-1.21	-0.36	-0.38
O59	-0.69	-1.23	-0.76	-0.69	-1.23	-0.76	-0.69	-1.23	-0.76	-0.69
O60	-0.73	-1.24	-0.78	-0.73	-1.24	-0.78	-0.73	-1.24	-0.78	-0.73
O61	-0.70	-1.22	-0.76	-0.70	-1.22	-0.76	-0.70	-1.22	-0.76	-0.70
E62	-0.54	-0.29	-0.76	-0.54	-0.29	-0.76	-0.54	-0.29	-0.76	-0.54
E63	-0.50	-0.22	-0.74	-0.50	-0.22	-0.74	-0.50	-0.22	-0.74	-0.50
E64	-0.53	-0.27	-0.76	-0.53	-0.27	-0.76	-0.53	-0.27	-0.76	-0.53
Dy65	2.38	2.13	2.49	2.38	2.13	2.49	2.38	2.13	2.49	2.38

Table S23. Calculated densities ($\rho(\boldsymbol{r})$), Laplacians ($\nabla^2\rho(\boldsymbol{r})$) and delocalization indices (*DI*) for the selected bond critical points (BCP) of **1**, **1**$_O$, **1**$_S$, **1**$_{Se}$, and **1**$_{Te}$.

	1			**1**$_O$			**1**$_S$			**1**$_{Se}$			**1**$_{Te}$		
BCP	$\rho(\boldsymbol{r})$	$\nabla^2\rho(\boldsymbol{r})$	***DI***	$\rho(\boldsymbol{r})$	$\nabla^2\rho(\boldsymbol{r})$	***DI***	$\rho(\boldsymbol{r})$	$\nabla^2\rho(\boldsymbol{r})$	***DI***	$\rho(\boldsymbol{r})$	$\nabla^2\rho(\boldsymbol{r})$	***DI***	$\rho(\boldsymbol{r})$	$\nabla^2\rho(\boldsymbol{r})$	***DI***
Dy65-N57	0.049	0.040	0.236	0.042	0.135	0.202	0.044	0.138	0.217	0.045	0.140	0.226	0.045	0.138	0.229
Dy65-N58	0.043	0.144	0.221	0.041	0.134	0.207	0.041	0.134	0.214	0.040	0.131	0.214	0.041	0.132	0.222
Dy65-O59	0.059	0.217	0.277	0.054	0.201	0.265	0.053	0.199	0.258	0.051	0.189	0.251	0.053	0.200	0.259
Dy65-O60	0.059	0.218	0.287	0.054	0.197	0.265	0.057	0.208	0.278	0.055	0.201	0.271	0.055	0.204	0.278
Dy65-O61	0.055	0.207	0.264	0.054	0.197	0.265	0.054	0.199	0.263	0.051	0.192	0.249	0.053	0.195	0.257
Dy65-E62	0.042	0.088	0.298	0.053	0.192	0.261	0.039	0.080	0.287	0.036	0.061	0.305	0.029	0.039	0.301
Dy65-E63	0.039	0.082	0.275	0.056	0.204	0.278	0.041	0.085	0.300	0.037	0.063	0.313	0.031	0.041	0.314
Dy65-E64	0.040	0.086	0.293	0.053	0.194	0.263	0.038	0.080	0.286	0.036	0.061	0.307	0.030	0.039	0.309

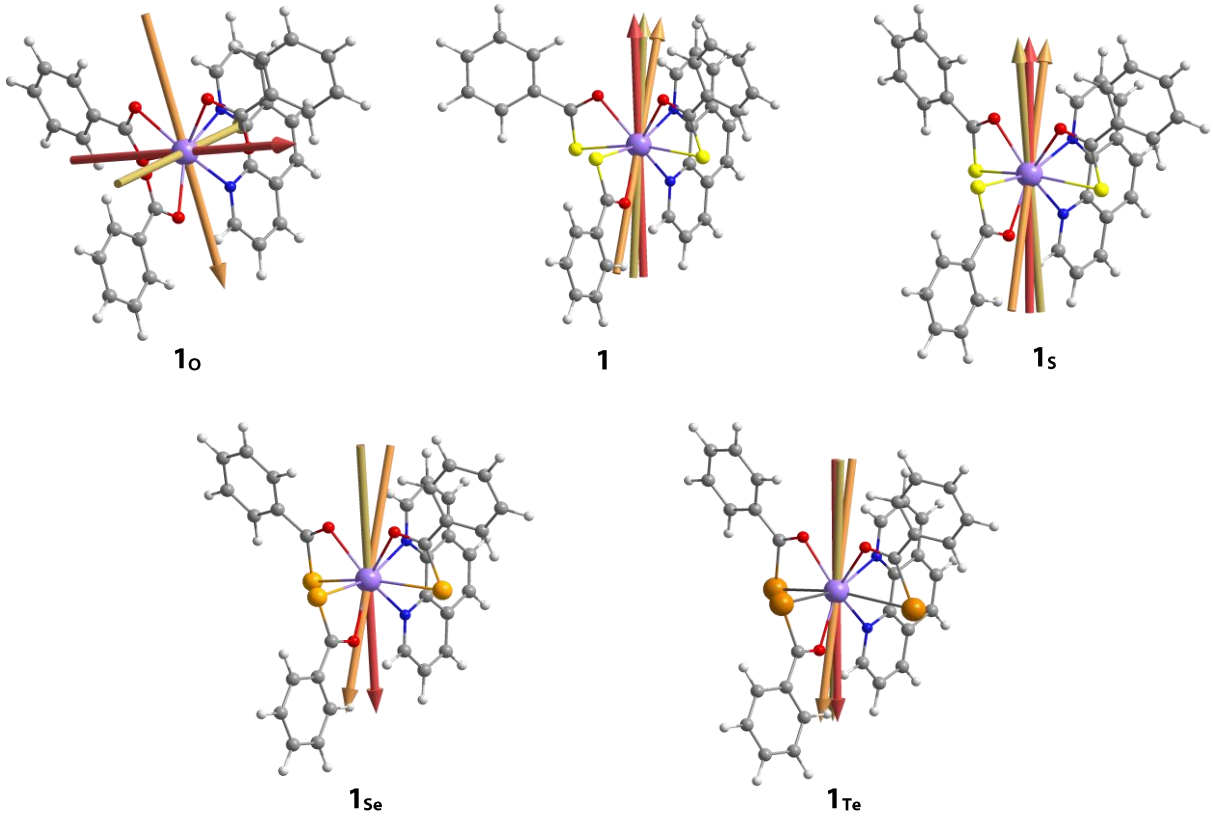

Figure S9. Main magnetic axes for the three first KD of the ground multiplet $^6H_{15/2}$ of Dy^{3+} ion in **1**, **1O**, **1S**, **1Se**, and **1Te**. Color coding for axes: red = the ground KD, orange = the first excited KD, yellow = the second excited KD.

Table S24. Excitation energies (cm^{-1}) for the first singlet (S*) and triplet (T*) excited states of tba^-_O, tba^-_S, tba^-_{Se}, tba^-_{Te}, and phen calculated at the CAM-B3LYP and LC-ωPBE exchange-correlation functionals in conjunction with different basis sets.

		CAM-B3LYP			
	ba⁻	**tba⁻**	**seba⁻**	**teba⁻**	**phen**
S* (TZVP)	-	24805.572	-	-	-
T* (TZVP)	-	22808.544	-	-	-
S* def2-TZVPP	35380.303	25053.990	22627.069	20117.879	35484.348
T* def2-TZVPP	28941.581	22923.075	20907.496	18768.514	22388.329
S* (def2-QZVPPD)	35539.194	24933.814	22538.348	19949.309	35386.755
T* (def2-QZVPPD)	28844.795	23059.382	21012.348	18709.636	22361.713
		LC-ωPBE			
	ba^-_O	**tba⁻**	**seba⁻**	**teba⁻**	**phen**
S* (TZVP)	-	28606.861	-	-	-
T* (TZVP)	-	24151.456	-	-	-
S* def2-TZVPP	38942.852	28705.261	26590.476	24358.741	37517.671
T* def2-TZVPP	25587.929	24015.149	22810.157	21661.624	19254.866
S* (def2-QZVPPD)	38999.311	28351.990	26323.507	24088.545	37432.983
T* (def2-QZVPPD)	25481.464	23938.526	22725.469	21436.595	19200.021

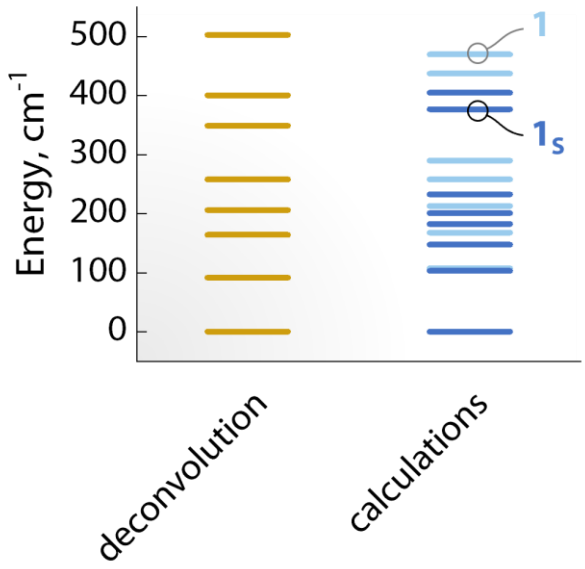

Figure S10. Comparison of the *mj* levels (KDs) of the ground $^{6}H_{15/2}$ multiplet of Dy^{3+} as obtained from the deconvolution of the $^{4}F_{5/2} \rightarrow {}^{6}H_{15/2}$ transition (yellow) and those calculated (light blue – **1**; dark blue – $\mathbf{1}_S$).

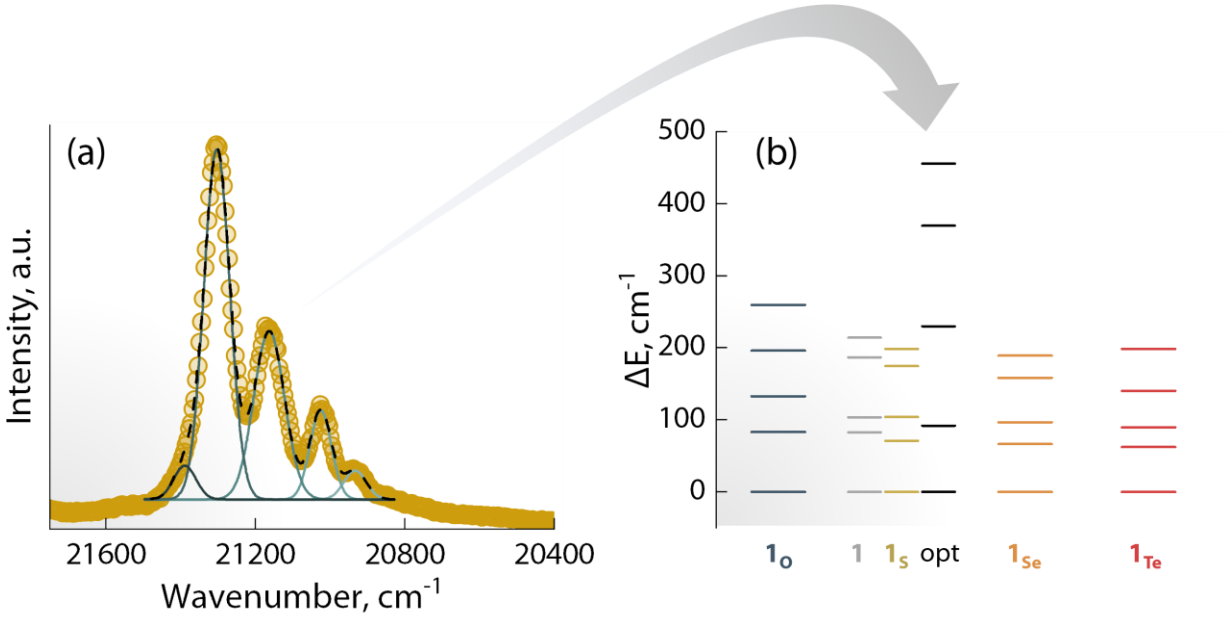

Figure S11. a) Deconvolution of the $^{6}H_{15/2} \rightarrow {}^{4}F_{5/2}$ transition observed in the excitation spectrum in **Figure 4a** of the main manuscript. Therein, the yellow points are the recorded spectrum, the blue solid lines are the main components of the deconvolution, and the dashed black line is the resulting simulated spectrum. **b)** Comparison of the relative position of the $^{4}F_{5/2}$ *mj* states for the different complexes explored. The values for $\mathbf{1_O}$, **1**, $\mathbf{1_S}$, $\mathbf{1_{Se}}$, and $\mathbf{1_{Te}}$ were obtained from Tables S9-S13. opt = optical.

Table S25. Optimized geometry for $\mathbf{1_o}$ obtained from the DFT calculations.

C	0.62119	-2.44896	-1.00470
C	0.71157	-3.86621	-1.44158
C	1.00359	-4.86206	-0.51470
H	1.17094	-4.57567	0.51666
C	1.07734	-6.18481	-0.92113
H	1.30631	-6.96194	-0.20047
C	0.86051	-6.51461	-2.25341
H	0.92002	-7.54996	-2.57109
C	0.57075	-5.52085	-3.18031
H	0.40649	-5.78031	-4.22021
C	0.49606	-4.19751	-2.77578
H	0.27688	-3.40195	-3.47785
C	2.97846	0.98294	0.19687
C	4.38407	1.41165	0.39710
C	4.88656	1.59210	1.68191
H	4.23244	1.41471	2.52681
C	6.20123	1.99127	1.86045
H	6.59466	2.13242	2.86086
C	7.01540	2.21034	0.75605
H	8.04453	2.52257	0.89645
C	6.51488	2.03031	-0.52747
H	7.15237	2.20163	-1.38747
C	5.20051	1.63134	-0.70835
H	4.78396	1.48281	-1.69728
C	-1.09113	2.32879	-1.01576
C	-1.91086	3.48567	-1.45822
C	-2.31187	4.44704	-0.53568
H	-2.00496	4.33310	0.49707
C	-3.08383	5.52131	-0.94824
H	-3.39589	6.27236	-0.23116
C	-3.45548	5.63714	-2.28212
H	-4.05816	6.47928	-2.60458
C	-3.05422	4.67862	-3.20457
H	-3.34180	4.77380	-4.24565
C	-2.28260	3.60328	-2.79402
H	-1.95163	2.84408	-3.49254
C	-2.68348	-0.93023	-1.19027
H	-2.15706	-0.75682	-2.12190
C	-4.00365	-1.39411	-1.16822
H	-4.51837	-1.58705	-2.10072
C	-4.61663	-1.59339	0.04223
H	-5.63932	-1.95137	0.09765
C	-3.91259	-1.33142	1.22943
C	-2.58807	-0.86809	1.10727
C	-4.48093	-1.51463	2.52566
H	-5.50254	-1.87137	2.59710
C	-3.76215	-1.25016	3.64160
H	-4.19671	-1.39062	4.62525
C	-2.41671	-0.78106	3.55435

C	-1.82306	-0.58773	2.29171
C	-1.63544	-0.49645	4.68667
H	-2.05995	-0.63365	5.67567
C	-0.34973	-0.05071	4.52442
H	0.28039	0.17749	5.37465
C	0.15554	0.11125	3.22844
H	1.16742	0.45966	3.05211
N	-2.00218	-0.67641	-0.08958
N	-0.55689	-0.14788	2.14886
O	0.32477	-1.55370	-1.84751
O	2.22972	0.77657	1.20050
O	-0.75598	1.44296	-1.85377
O	0.82775	-2.15344	0.20754
O	2.53223	0.82321	-0.97306
O	-0.74702	2.23263	0.19807
Dy	0.39122	0.16622	-0.19752

Table S26. Optimized geometry for $\mathbf{1}_S$ obtained from the DFT calculations.

C	0.57034	-2.60965	1.07977
C	1.13162	-3.78956	1.77925
C	1.09435	-5.06402	1.21809
H	0.63103	-5.19367	0.24693
C	1.64086	-6.13940	1.89820
H	1.60894	-7.12931	1.45737
C	2.22617	-5.95080	3.14405
H	2.65140	-6.79468	3.67630
C	2.26357	-4.68243	3.70985
H	2.71462	-4.53589	4.68489
C	1.71960	-3.60516	3.03096
H	1.73153	-2.60845	3.45482
C	-3.26291	0.09082	0.33373
C	-4.73554	0.10691	0.18543
C	-5.28714	0.04315	-1.09416
H	-4.62092	-0.01903	-1.94514
C	-6.66093	0.05576	-1.26415
H	-7.08398	0.00425	-2.26109
C	-7.49642	0.13371	-0.15707
H	-8.57272	0.14401	-0.28958
C	-6.95314	0.19776	1.11988
H	-7.60380	0.25856	1.98474
C	-5.57950	0.18362	1.29161
H	-5.14066	0.23208	2.28122
C	0.75690	2.60847	1.03146
C	1.37935	3.75782	1.72876
C	1.40993	5.03149	1.16546
H	0.95706	5.18355	0.19262
C	2.00864	6.07822	1.84629
H	2.02946	7.06786	1.40423
C	2.57852	5.86156	3.09476
H	3.04438	6.68327	3.62766
C	2.54846	4.59387	3.66251
H	2.98755	4.42579	4.63952
C	1.95235	3.54508	2.98299
H	1.91096	2.54986	3.40845
C	3.05734	-0.12557	0.16167
H	2.78038	-0.11029	1.20938
C	4.39563	-0.18892	-0.23964
H	5.17676	-0.22374	0.50890
C	4.68651	-0.20511	-1.57962
H	5.71284	-0.25321	-1.92790
C	3.64153	-0.15820	-2.51691
C	2.32540	-0.09682	-2.01893
C	3.86525	-0.16927	-3.92632
H	4.88671	-0.21679	-4.28734
C	2.82773	-0.12111	-4.79367
H	3.00070	-0.12887	-5.86420
C	1.48149	-0.05824	-4.32356
C	1.22332	-0.04736	-2.93869
C	0.37711	-0.00577	-5.18942
H	0.53923	-0.01218	-6.26207

C	-0.88826	0.05323	-4.66543
H	-1.76226	0.09534	-5.30287
C	-1.04777	0.05904	-3.27559
H	-2.02953	0.10336	-2.81738
N	2.05731	-0.08150	-0.69867
N	-0.02807	0.01031	-2.43862
O	0.70572	-1.48305	1.61428
O	-2.55795	0.05443	-0.71244
O	0.82906	1.47783	1.57044
S	-0.23899	-2.76526	-0.43465
S	-2.51508	0.11647	1.87863
S	-0.04150	2.79964	-0.48451
Dy	-0.33852	0.02834	0.09276

Table S27. Optimized geometry for $\mathbf{1}_{Se}$ obtained from the DFT calculations.

C	0.85937	2.61268	-1.10128
C	1.42560	3.72720	-1.89146
C	1.44416	5.03658	-1.41596
H	1.02288	5.24541	-0.43910
C	1.99115	6.04853	-2.18645
H	2.00293	7.06564	-1.81166
C	2.52005	5.76183	-3.43886
H	2.94446	6.55659	-4.04253
C	2.50162	4.45850	-3.92009
H	2.90812	4.23569	-4.90024
C	1.95870	3.44413	-3.15039
H	1.92752	2.42204	-3.50765
C	-3.17332	0.04702	-0.17685
C	-4.63259	0.07426	0.05721
C	-5.10365	0.11349	1.37062
H	-4.38572	0.12380	2.18074
C	-6.46369	0.13994	1.62555
H	-6.82266	0.17098	2.64818
C	-7.36776	0.12690	0.57085
H	-8.43361	0.14742	0.76985
C	-6.90599	0.08773	-0.73881
H	-7.60996	0.07748	-1.56299
C	-5.54596	0.06187	-0.99531
H	-5.17188	0.03151	-2.01223
C	0.78068	-2.64992	-1.07157
C	1.30217	-3.79216	-1.85307
C	1.26432	-5.09834	-1.37010
H	0.83204	-5.28368	-0.39331
C	1.76994	-6.13690	-2.13346
H	1.73772	-7.15146	-1.75301
C	2.31357	-5.87999	-3.38602
H	2.70548	-6.69540	-3.98409
C	2.35137	-4.57983	-3.87465
H	2.76936	-4.37999	-4.85493
C	1.84974	-3.53911	-3.11219
H	1.86238	-2.51872	-3.47535
C	3.20090	-0.04151	-0.09403
H	2.91881	-0.04278	-1.14023
C	4.54242	-0.05717	0.29913
H	5.31956	-0.07057	-0.45423
C	4.84136	-0.05536	1.63735
H	5.87062	-0.06746	1.98000
C	3.80087	-0.03770	2.58038
C	2.47975	-0.02239	2.09157
C	4.03560	-0.03548	3.98794
H	5.06092	-0.04776	4.34086
C	3.00373	-0.01844	4.86286
H	3.18469	-0.01706	5.93209
C	1.65292	-0.00227	4.40239
C	1.38348	-0.00334	3.01929
C	0.55472	0.01521	5.27728
H	0.72586	0.01654	6.34853

C	-0.71605	0.02997	4.76314
H	-1.58593	0.04327	5.40752
C	-0.88625	0.02747	3.37476
H	-1.87219	0.03849	2.92383
N	2.20408	-0.02454	0.77193
N	0.12699	0.01153	2.52881
O	0.95608	1.45087	-1.54883
O	-2.40659	0.04727	0.81858
O	0.92308	-1.49660	-1.52798
Se	0.00176	2.89802	0.54266
Se	-2.44437	0.01425	-1.89512
Se	-0.08830	-2.88848	0.57444
Dy	-0.18418	0.00287	-0.012817

Table S28. Optimized geometry for $\mathbf{1}_{Te}$ obtained from the DFT calculations.

C	0.26270	2.77462	-1.14318
C	0.60153	3.90704	-2.02723
C	0.29689	5.22471	-1.69335
H	-0.21259	5.42520	-0.75681
C	0.63992	6.25725	-2.54900
H	0.40030	7.28041	-2.28326
C	1.28611	5.98173	-3.74783
H	1.55000	6.79136	-4.41937
C	1.59000	4.66936	-4.08935
H	2.08724	4.45399	-5.02846
C	1.25231	3.63562	-3.23370
H	1.47272	2.60469	-3.48250
C	-3.03103	-0.82930	-0.23515
C	-4.45369	-1.11587	0.02985
C	-4.96867	-0.84900	1.30078
H	-4.31201	-0.42477	2.04998
C	-6.29903	-1.10372	1.58344
H	-6.69529	-0.88362	2.56842
C	-7.12685	-1.63873	0.60418
H	-8.16872	-1.84155	0.82628
C	-6.62053	-1.90994	-0.66088
H	-7.26455	-2.32794	-1.42596
C	-5.29304	-1.64474	-0.94871
H	-4.88717	-1.84805	-1.93377
C	1.76158	-2.28260	-1.00614
C	2.68654	-3.08990	-1.82571
C	3.10146	-4.36209	-1.43849
H	2.72783	-4.77660	-0.50821
C	3.97586	-5.08200	-2.23411
H	4.29524	-6.07113	-1.92667
C	4.43954	-4.53905	-3.42606
H	5.12105	-5.10613	-4.05060
C	4.02698	-3.27206	-3.82085
H	4.38294	-2.85173	-4.75475
C	3.15658	-2.54826	-3.02501
H	2.81637	-1.56198	-3.31627
C	3.15548	0.95349	0.20914
H	2.96810	0.86551	-0.85459
C	4.39710	1.36990	0.69698
H	5.19070	1.61145	0.00164
C	4.57932	1.46219	2.05314
H	5.52920	1.78133	2.46878
C	3.52230	1.13777	2.91864
C	2.30616	0.72951	2.33655
C	3.64083	1.20375	4.33906
H	4.58627	1.52130	4.76475
C	2.59852	0.87657	5.13694
H	2.69121	0.92491	6.21631
C	1.35267	0.45774	4.58065
C	1.19710	0.38848	3.18182
C	0.25058	0.10540	5.37559
H	0.33616	0.14790	6.45615

C	-0.91559	-0.28927	4.77184
H	-1.78490	-0.57166	5.35202
C	-0.97845	-0.32592	3.37597
H	-1.88048	-0.62979	2.85713
N	2.14396	0.64554	1.00076
N	0.04055	0.00317	2.60223
O	0.66663	1.63689	-1.45385
O	-2.28574	-0.57188	0.73958
O	1.52154	-1.11152	-1.35786
Te	-0.87872	2.98590	0.60764
Te	-2.21696	-0.78925	-2.16214
Te	0.81900	-3.02132	0.72108
Dy	-0.08213	-0.05024	0.05356

6. Simulation of the thermometric performance

As explained in the main text, the luminescence thermometry approach proposed in this study relies on the temperature-driven redistribution of the electron populations within the 5 *mj* levels of the Dy^{3+}:$^4F_{9/2}$ emitting state (see also **Figure 6c**). Electron population redistribution within two thermally coupled energy levels can be described by a Boltzmann function as follows:

$$\frac{N_2}{N_1} = \left(\frac{g_2}{g_1}\right) \exp\left(\frac{-\Delta E_{12}}{k_B T}\right) \tag{S6}$$

Where ΔE_{12} is the energy difference between the two levels, k_B is the Boltzmann constant, T is the temperature, g_i and N_i are, respectively, the degeneracy and the electron population of the i-th level. Since all the *mj* levels are doubly degenerate (Kramers doublets) in Dy^{3+} under no applied magnetic field, the ratio between the degeneracies is equal to unity. It is therefore possible to build a system of equations like the one below to describe the electron population distribution at a given temperature:

$$\begin{cases} N_1 + N_2 + N_3 + N_4 + N_5 = 1 \\ N_2 = N_1 \exp\left(\frac{-\Delta E_{12}}{k_B T}\right) \\ N_3 = N_2 \exp\left(\frac{-\Delta E_{23}}{k_B T}\right) \\ N_4 = N_3 \exp\left(\frac{-\Delta E_{34}}{k_B T}\right) \\ N_5 = N_4 \exp\left(\frac{-\Delta E_{45}}{k_B T}\right) \end{cases} \tag{S7}$$

Solving the system of equations, leads to:

$$\begin{cases} N_1 = \dfrac{1}{1 + \exp\left(\frac{-\Delta E_{12}}{k_B T}\right) + \exp\left(\frac{-\Delta E_{13}}{k_B T}\right) + \exp\left(\frac{-\Delta E_{14}}{k_B T}\right) + \exp\left(\frac{-\Delta E_{15}}{k_B T}\right)} \\ N_i = \dfrac{\exp\left(\frac{-\Delta E_{1i}}{k_B T}\right)}{1 + \exp\left(\frac{-\Delta E_{12}}{k_B T}\right) + \exp\left(\frac{-\Delta E_{13}}{k_B T}\right) + \exp\left(\frac{-\Delta E_{14}}{k_B T}\right) + \exp\left(\frac{-\Delta E_{15}}{k_B T}\right)} \end{cases} \tag{S8}$$

Considering the low temperatures at which the study is conducted, in a first approximation the thermometric performance will be determined by the electron population redistribution within the first two *mj* states. Hence, in Figure 6d of the main text the trend of N_2/N_1 vs temperature has been reported.

References

1. V. V. Savant, J. Gopalakrishnan, C. C. Patel *Inorg. Chem.*, 1970, **9,** 748-751.
2. D. Reta, N. F. Chilton, *Phys. Chem. Chem. Phys.*, **2019,** *21*, 23567-23575.
3. C. D. S. Brites, A. Millán and L. D. Carlos, in Handbook on the Physics and Chemistry of Rare Earths, Vol. 49 (Eds: J.-C. G. Bünzli, V. K. Pecharsky), Elsevier Science, B. V., Amsterdam 2016, p. 339.
4. Gaussian 16, Revision C.01, M. J. Frisch, G. W. Trucks, H. B. Schlegel, G. E. Scuseria, M. A. Robb, J. R. Cheeseman, G. Scalmani, V. Barone, G. A. Petersson, H. Nakatsuji, X. Li, M. Caricato, A. V. Marenich, J. Bloino, B. G. Janesko, R. Gomperts, B. Mennucci, H. P. Hratchian, J. V. Ortiz, A. F. Izmaylov, J. L. Sonnenberg, D. Williams-Young, F. Ding, F. Lipparini, F. Egidi, J. Goings, B. Peng, A. Petrone, T. Henderson, D. Ranasinghe, V. G. Zakrzewski, J. Gao, N. Rega, G. Zheng, W. Liang, M. Hada, M. Ehara, K. Toyota, R. Fukuda, J. Hasegawa, M. Ishida, T. Nakajima, Y. Honda, O. Kitao, H. Nakai, T. Vreven, K. Throssell, J. A. Montgomery, Jr., J. E. Peralta, F. Ogliaro, M. J. Bearpark, J. J. Heyd, E. N. Brothers, K. N. Kudin, V. N. Staroverov, T. A. Keith, R. Kobayashi, J. Normand, K. Raghavachari, A. P. Rendell, J. C. Burant, S. S. Iyengar, J. Tomasi, M. Cossi, J. M. Millam, M. Klene, C. Adamo, R. Cammi, J. W. Ochterski, R. L. Martin, K. Morokuma, O. Farkas, J. B. Foresman, and D. J. Fox, Gaussian, Inc., Wallingford CT, 2016.
5. M. Ernzerhof and G. E. Scuseria, *J. Chem. Phys.*, 1999, **110**, 5029–5036.
6. C. Adamo and V. Barone, *J. Chem. Phys.*, 1999, **110**, 6158–6170.
7. S. Grimme, J. Antony, S. Ehrlich and H. Krieg, *J. Chem. Phys.*, 2010, **132**, 154104.
8. S. Grimme, S. Ehrlich and L. Goerigk, *J. Comput. Chem.*, 2011, **32**, 1456–1465
9. A. Schäfer, C. Huber and R. Ahlrichs, *J. Chem. Phys.*, 1994, **100**, 5829–5835.
10. K. Eichkorn, F. Weigend, O. Treutler and R. Ahlrichs, *Theor. Chem. Acc.*, 1997, **97**, 119–124.
11. T. R. Cundari and W. J. Stevens, *J. Chem. Phys.*, 1993, **98**, 5555–5565.
12. P. Pollak, F. Weigend, *J. Chem. Theory Comput.* 2017, **13**, 3696-3705.
13. R.F.W. Bader, *Atoms in Molecules: A Quantum Theory"*, Oxford University Press, Oxford (1990)
14. AIMAll (Version 19.10.12), Todd A. Keith, TK Gristmill Software, Overland Park KS, USA, 2019.
15. A. Kerridge, *Chem. Commun.*, 2017, **53**, 6685.
16. T. Yanai, D. P. Tew and N. C. Handy, *Chem. Phys. Lett.*, 2004, **393**, 51–57.
17. O. A. Vydrov, J. Heyd, A. V. Krukau and G. E. Scuseria, *J. Chem. Phys.*, 2006, **125**, 074106.
18. O. A. Vydrov and G. E. Scuseria, *J. Chem. Phys.*, 2006, **125**, 234109.
19. O. A. Vydrov, G. E. Scuseria and J. P. Perdew, *J. Chem. Phys.*, 2007, **126**, 154109.
20. F. Weigend and R. Ahlrichs, *Phys. Chem. Chem. Phys.*, 2005, **7**, 3297–3305.
21. B. O. Roos, P. R. Taylor and P. E. M. Sigbahn, *Chem. Phys.*, 1980, **48**, 157–173
22. P. Siegbahn, A. Heiberg, B. Roos and B. Levy, *Phys. Scr.*, 1980, **21**, 323–327.
23. B. O. Roos, R. Lindh, P. Å. Malmqvist, V. Veryazov, P.-O. Widmark, *Multiconfigurational Quantum Chemistry*, John Wiley & Sons, Ltd, 1st edn., 2016.
24. B. A. Hess, *Phys. Rev. A*, 1986, **33**, 3742–3748.
25. M. Douglas and N. M. Kroll, *Ann. Phys.*, 1974, **82**, 89–155.
26. B. A. Heß, C. M. Marian, U. Wahlgren and O. Gropen, *Chem. Phys. Lett.*, 1996, **251**, 365–371.
27. I. Fdez. Galván, M. Vacher, A. Alavi, C. Angeli, F. Aquilante, J. Autschbach, J. J. Bao, S. I. Bokarev, N. A. Bogdanov, R. K. Carlson, L. F. Chibotaru, J. Creutzberg, N. Dattani, M. G. Delcey, S. S. Dong, A. Dreuw, L. Freitag, L. M. Frutos, L. Gagliardi, F. Gendron, A. Giussani, L. González, G. Grell, M. Guo, C. E. Hoyer, M. Johansson, S. Keller, S. Knecht, G. Kovačević, E. Källman, G. Li Manni, M. Lundberg, Y. Ma, S. Mai, J. P. Malhado, P. Å. Malmqvist, P. Marquetand, S. A. Mewes, J. Norell, M. Olivucci, M. Oppel, Q. M. Phung, K. Pierloot, F. Plasser, M. Reiher, A. M. Sand, I. Schapiro, P. Sharma, C. J. Stein, L. K. Sørensen, D. G. Truhlar, M. Ugandi, L. Ungur, A. Valentini, S. Vancoillie, V. Veryazov, O. Weser, T. A. Wesołowski, P.-O. Widmark, S. Wouters, A. Zech, J. P. Zobel and R. Lindh, *J. Chem. Theory Comput.*, 2019, **15**, 5925–5964.
28. B. O. Roos, R. Lindh, P.-Å. Malmqvist, V. Veryazov, P.-O. Widmark and A. C. Borin, *J. Phys. Chem. A*, 2008, **112**, 11431–11435.

29. B. O. Roos, R. Lindh, P.-Å. Malmqvist, V. Veryazov and P.-O. Widmark, *J. Phys. Chem. A*, 2004, **108**, 2851–2858
30. D. Peng, M. Reiher, *Theor. Chem. Acc.* 2012, **131**, 1081.
31. Filatov, *J. Chem. Phys.* 2006, **125**, 107101
32. W. Kutzelnigg, W. Liu, *J. Chem. Phys.* 2005, **123**, 241102.
33. L. F. Chibotaru and L. Ungur, *J. Chem. Phys.*, 2012, **137**, 064112.
34. L. Ungur and L. F. Chibotaru, *Chem. - A Eur. J.*, 2017, **23**, 3708–3718.
35. L. Ungur, M. Thewissen, J.-P. Costes, W. Wernsdorfer and L. F. Chibotaru, *Inorg. Chem.*, 2013, **52**, 6328–6337.